Redox Biology 82 (2025) 103597

Contents lists available at ScienceDirect

Redox Biology

journal homepage: www.elsevier.com/locate/redox

Hippo pathway activation mediates cardiomyocyte ferroptosis to promote dilated cardiomyopathy through downregulating NFS1

Gang She [a,e,1], Xia-Xia Hai [a,1], Li-Ye Jia [b,1], Yong-Jian Zhang [c], Yu-Jie Ren [d], Zheng-Da Pang [a], Lin-Hong Wu [a], Meng-Zhuan Han [a], Yu Zhang [a], Jing-Jing Li [a], Ru-Yue Bai [a], Bao-Chang Lai [g], Yi-Yi Yang [a], Junichi Sadoshima [h], Xiao-Jun Du [a,f,*], Xiu-Ling Deng [a,**], Yi Zhang [a,***]

[a] Department of Physiology and Pathophysiology, School of Basic Medical Sciences, Xi'an Jiaotong University Health Science Center, 76 West Yanta Road, Xi'an, 710061, Shaanxi, China
[b] School of Nursing and Rehabilitation, Xi'an Medical University, 1 Xinwang Road, Xi'an, 710021, Shaanxi, China
[c] Department of Cardiovascular Surgery, The First Affiliated Hospital of Xi'an Jiaotong University, 88 Zhuque Street, Xi'an, 710061, Shaanxi, China
[d] Department of Pathology, Xi'an People's Hospital (Xian Fourth Hospital), Affiliated to Xi'an Jiaotong University Health Science Center, 21 Jiefang Road, Xi'an, 710005, Shaanxi, China
[e] Department of Cardiology, The Second Affiliated Hospital of Xi'an Jiaotong University, Xi'an, 710061, Shaanxi, China
[f] Baker Heart and Diabetes Institute, 75 Commercial Road, Melbourne, Victoria, 3004, Australia
[g] Cardiovascular Research Centre, School of Basic Medical Sciences, Xi'an Jiaotong University Health Science Center, 76 West Yanta Road, Xi'an, 710061, Shaanxi, China
[h] Department of Cell Biology and Molecular Medicine, Rutgers New Jersey Medical School, New Jersey, United States of America

ARTICLE INFO

Keywords:
Dilated cardiomyopathy
Hippo pathway
Ferroptosis
NFS1
Iron-sulfur cluster

ABSTRACT

Cardiomyocyte loss by regulated death modes, like apoptosis and ferroptosis, has been implicated in the development of dilated cardiomyopathy (DCM). It remains unclear whether cardiomyocyte ferroptosis occurs as a consequence of Hippo pathway activation. Using a mouse model of DCM by overexpression of Mst1 transgene (Mst1-TG) leading to Hippo pathway activation, we showed that cardiomyocyte ferroptosis was evident by transcriptomic profiles, elevated mitochondrial Fe^{2+} content, increased levels of lipid peroxidation and obvious mitochondrial damage. Transcriptome revealed significant alterations of genes participating in iron metabolism and lipid peroxidation. Treatment of Mst1-TG mice with the ferroptosis inhibitor ferrostatin-1 reduced cardiomyocyte ferroptosis and improved cardiac function. Using heart samples from human patients with DCM, we also found significant cardiomyocyte loss and lipid peroxidation. In cultured cardiomyocytes, ferroptosis was induced by treatment with erastin or YAP inhibitor verteporfin, and cell ferroptosis under these conditions was largely prevented by either iron chelation or Mst1 gene knockdown. In a strain of transgenic mice with cardiomyocyte inactivation of Mst1 (dnMst1-TG), erastin-induced ferroptosis and cardiac dysfunction, seen in control mice, were mitigated. Mechanistically, nuclear YAP and YY1 were shown to interact and bind to the *Nfs1* promoter, thus mediating downregulation of *Nfs1* (encoding cysteine desulfurase). Subsequent inhibition of iron-sulfur cluster (ISC) biosynthesis promoted cardiomyocyte ferroptosis and DCM phenotype. Restoration of *Nfs1* expression was achieved by treatment of Mst1-TG mice with AAV9-*Nfs1* virus, which alleviated ferroptosis, mitochondrial damage and DCM phenotype. In conclusion, in the DCM model with Hippo pathway activation, our findings unravel that NFS1 downregulation occurs and leads to insufficient ISC biosynthesis and cardiomyocyte ferroptosis. Our findings implicate that restoration of cardiomyocyte NFS1 level may represent a new therapeutic strategy for DCM.

* Corresponding author. Department of Physiology and Pathophysiology, School of Basic Medical Sciences, Xi'an Jiaotong University Health Science Center, 76 West Yanta Road, Xi'an, 710061, Shaanxi, China.xiao-jun.du@baker.edu.au
** Corresponding author.
*** Corresponding author.
E-mail addresses: dengxl@mail.xjtu.edu.cn (X.-L. Deng), zhangyixjtu@xjtu.edu.cn (Y. Zhang).
[1] These authors contributed equally to this work.

https://doi.org/10.1016/j.redox.2025.103597
Received 2 February 2025; Received in revised form 13 March 2025; Accepted 13 March 2025
Available online 14 March 2025
2213-2317/© 2025 The Authors. Published by Elsevier B.V. This is an open access article under the CC BY-NC-ND license (http://creativecommons.org/licenses/by-nc-nd/4.0/).

1. Introduction

Ferroptosis is an iron-dependent non-apoptotic cell death mode that is driven by aberrant accumulation of peroxidized polyunsaturated phospholipids [1]. Mitochondrial iron overload induces excessive production of reactive oxygen species (ROS) and disrupts cellular defense against oxidative stress, particularly the glutathione (GSH)-dependent antioxidant system, and leads to lipid peroxidation and ferroptosis [2]. In cells undergoing ferroptosis, iron-overloaded mitochondria display distorted morphology, including increased density of the outer membrane and damaged cristae [3]. The role of cardiomyocyte ferroptosis in the development of heart disease has attracted increasing attention with reports showing involvement of ferroptosis in settings of doxorubicin-induced cardiomyopathy, myocardial ischemia and heart failure [4–6]. Currently, ferroptosis inhibitor iron chelator dexrazoxane is the only FDA-approved drug for treatment of chemotherapy-induced cardiomyopathy [7]. However, mechanisms mediating mitochondrial iron overload, mitochondrial damage, enhanced ROS production and cardiomyocyte ferroptosis are only partially understood.

Hippo signaling pathway plays a key role in the regulation of organ development [8]. The core components of Hippo pathway include upstream kinases of mammalian sterile 20-like kinase (Mst) and large tumor suppressor homolog (Lats), and downstream transcriptional co-regulator yes-associated protein (YAP). Nuclear YAP regulates expression of numerous genes via binding with various transcriptional factors like TEA-domain family member (TEAD) [9]. Phosphorylation of YAP at different sites regulates its intracellular localization. Canonical Mst/Lats-induced YAP phosphorylation at Ser127 site (Ser127-pYAP) inhibits YAP nuclear translocation together with increased cytoplasmic retention, ubiquitination and degradation [10,11]. Meanwhile, YAP is a substrate of some kinases including Src tyrosine kinase. Src phosphorylates YAP at Tyr357 site (Tyr357-pYAP) to enhance YAP nuclear entry [12,13]. Studies from this and other groups have shown that transcriptional activity of YAP in cardiomyocytes is cardio-protective whilst Hippo pathway activation or YAP/TEAD inhibition mediates development of dilated cardiomyopathy (DCM) or drug-induced cardiotoxicity [10,14,15]. Using a mouse model with enhanced Hippo signaling due to cardiomyocyte-restricted overexpression of Mst1 transgene (Mst1-TG), we demonstrated, in young (3-week-old) and adult mice, profound downregulation of mitochondrion-associated genes, mitochondrial damage and DCM phenotype [10]. In several clinical studies, analysis of cardiac samples from human patients with ischemic or non-ischemic cardiomyopathy, heart failure or arrhythmic cardiomyopathy, revealed elevated levels of phosphorylated Lats and Ser127-pYAP, and downregulation of TEAD1, suggesting Hippo pathway activation [16–18]. Cardiomyocyte loss has been implicated as a key mechanism in the development of cardiomyopathy and heart failure [4]. However, it remains unclear whether cardiomyocyte ferroptosis is involved in the occurrence of cardiomyopathy associated with Hippo pathway activation.

Iron turnover and metabolism occur actively in mitochondrion, where iron is primarily used to synthesize iron-sulfur clusters (ISCs) and heme [19]. ISC is an essential cofactor for the function of numerous iron-sulfur proteins in many biochemical pathways such as the electron transport chain, energy metabolism and DNA synthesis or repair [20]. Cysteine desulfurase (NFS1) is a rate-limiting mitochondrial enzyme in ISC assembling by providing sulfur from cysteine, and plays a key role in the maintenance of mitochondrial iron homeostasis [21]. In cancer cells, NFS1 activity determines the degree of the iron-starvation-response and the sensitivity of cells to ferroptosis [22,23]. There has been no report thus far on whether activation of cardiomyocyte Hippo pathway affects NFS1 expression and hence ferroptosis.

Our central hypothesis here was that in the cardiomyopathy model with enhanced Hippo pathway activity, cardiomyocyte ferroptosis occurs due to suppressed expression of NFS1, which diminishes ISC biosynthesis but enhances ROS generation and lipid peroxidation. We addressed this hypothesis using two strains of TG mice with cardiac Hippo pathway signaling either activated (Mst1-TG) or diminished (dominant-negative mutant Mst1, dnMst1-TG). We also analyzed myocardial samples from clinical DCM patients for validation purpose. Ferroptosis inhibitors or inducer were tested both *in vitro* and *in vivo*. Finally, the effects of virally-mediated *Nfs1* gene transfer on ferroptosis and DCM phenotype were tested in the Mst1-TG mice.

2. Methods

2.1. Animals and drug treatment

We used Mst1-TG and dnMst1-TG mouse strains as well as their non-TG littermates (nTG). Both strains were in the same C57BL/6J genetic background and the transgene (Mst1 or dnMst1) was driven by α-myosin heavy chain (α-MHC) promoter, as previously reported [24,25] The genotype was determined by PCR of tail biopsy. Animals were housed in standard conditions. Two drugs were tested *in vivo*: ferroptosis inhibitor ferrostatin-1 (Fer-1, 1 mg/kg in corn oil, i.p., once every second day for 4 weeks) [26], and ferroptosis inducer erastin (20 mg/kg in corn oil, i.p., three times per week for 4 weeks) [27]. At the end of experiments, animals were under deep anesthesia (isoflurane inhalation at 4 %) and blood and hearts were collected for assays. All experimental protocols were approved by the Biomedical Animal Ethics Committee of Health Science Center, Xi'an Jiaotong University, and conformed to the Guide for the Care and Use of Laboratory Animals published by the National Institutes of Health (No. 2022-624).

2.2. Human heart samples

Cardiac samples of control human subjects were from autopsy donors provided by the Department of Pathology, the First Affiliated Hospital of Xi'an Jiaotong University. All six donors died of acute trauma without signs of heart disease. Myocardial samples of the left ventricle (LV) were obtained from DCM patients (n = 5) who received heart transplantation surgery. All patients were notified the nature of the study and expressed their willingness to participate through a consent form conformed to the principles outlined in the Declaration of Helsinki. Supplementary Table S1 contain information of the donors and patients. This study was approved by the Ethics Committee of the First Affiliated Hospital of Xi'an Jiaotong University (No. LLSBPJ-2024-003).

2.3. Echocardiography

Echocardiography was performed using a Vevo 3100 ultrasound machine (Visualsonics Inc, Toronto, Canada) with a MX550D transducer, as described previously [28]. Mice were anesthetized under 1–2 % isoflurane. Two-dimensional (2-D) short-axis image of the LV was obtained at the level of papillary muscles, and the 2-D image guided M-mode traces crossing the anterior and posterior walls were recorded. We measured from the M-mode tracings the LV wall thickness at the diastole and systole (WTd, WTs), and the LV internal dimensions at the diastole and systole (LVIDd, LVIDs). Fractional shortening (FS) was calculated as [(LVIDd-LVIDs)/LVIDd] × 100 %, and ejection fraction (EF) was calculated from LV diastolic and systolic volumes derived from LV dimensions. Wall thickening index (WTI) was calculated as [(WTs-WTd)/WTd] × 100 %, as previously described [29]. Images from 5 cardiac cycles were analyzed in a blinded fashion, and the average used.

2.4. Isolation of primary cardiomyocytes and virally mediated gene transfer

Primary neonatal rat ventricular myocytes (NRVMs) were isolated from 3-day-old Sprague-Dawley rats euthanized by cervical dislocation. Briefly, hearts were excised and thoroughly washed with PBS under

aseptic conditions. Ventricular tissues were minced and digested with buffer containing collagenase type II (1 mg/mL, Gibco, 17101015) for 3 min at 37 °C. The digestion was repeated 4–6 times until the digestion fluid became clear. Cardiomyocytes were enriched (>90 % purity) by a 2-h pre-plating step in 100-mm dishes in complete medium at 37 °C with 5 % CO_2 to remove fibroblasts. Unattached cardiomyocytes were collected, plated on dishes (Corning, NY, USA), and cultured overnight in DMEM with 0.1 mmol/L BrdU. To transfect cardiomyocytes with adenovirus (Ad) particles, Ad-Mst1-shRNA, Ad-Nfs1-shRNA or Ad-Nfs1 was added at the dose of 10^8 transduction unit (TU) per mL medium. At the end, the efficiency of transfection was evaluated by Western blotting.

2.5. Single-nucleus RNA sequencing

Single-nucleus RNA sequencing (snRNA-seq) was performed by the Novogene Co. Ltd, Tianjin, China [30]. The LV samples (30–50 mg each) were harvested from 3-month-old male Mst1-TG and nTG controls (n = 3 each), and cut into 1–2 mm^3 using chilled razor blades. In order to isolate nuclei, the tissue was suspended in a lysis buffer (for 5 min) and homogenized using a Dounce homogenizer. Intact nuclei were verified by SYBR Green II RNA Gel Stain. Resuspended nuclei were counted and pellets washed twice in a resuspension buffer. The resuspension solution was filtered with a 40 μm Flowmi cell strainer, and transferred to a 1.5 ml tube. Nuclei were counted again and incubated with DAPI (4′6-diamidino-2-phenylindole, dihydrochloride). To exclude debris or nuclei aggregates, fluorescence-activated cell sorting was performed with a BD Influx cell sorter (BD Biosciences), gating for DAPI positivity (for 1–1.5 h). Nuclei were collected, washed and then counted. 10 × Chromium single-cell gene expression technology (3′ v2 10 × Genomics) was used to generate single-indexed libraries as per the manufacturer's protocols. RNA sequencing was performed on a NovaSeq 6000 platform (Illumina).

SnRNA-seq bioinformatic analyses: Single nucleus sequencing reads were mapped to the *de novo* reference transcriptome using Cell Ranger v3 (10 × Genomics). All samples passed bioinformatics quality control. Expression of 50–8000 genes per nucleus was identified, and less than 30,000 unique molecular identifiers, both of which are indicators of good quality data (e.g. not suggesting a major contribution of droplet doublets). No mitochondrial RNA was detected. The raw gene × nucleus read counts were normalized using SCTransform. All samples were integrated with Seurat's integration anchors, using Canonical Correlation Analysis, and clustered using Seurat, as implemented in CReSCENT multi-sample pipeline. This pipeline included batch effect correction, data dimension reduction, cell clustering, and visualization using the t-Distributed Stochastic Neighbor Embedding (t-SNE). Cell identities were assigned to each cluster, comparing average gene expression profiles for each cluster against manually curated cardiac cell type signatures, using Gene Set Variation Analysis (GSVA). Cell identities were also cross-referenced with known markers.

Composition analysis: To identify group-difference in cell types, we applied the Bayesian method from scCODA v0.1.2. For this analysis, vascular smooth muscle cells were selected as a reference cell type with relatively invariant across samples.

Pathway analysis: Statistically significant DE genes were used to perform pathway analysis via EnrichR (https://maayanlab.cloud/Enrichr/). Pathway enrichment values were downloaded as.csv files and plots were generated in GraphPad Prism.

2.6. Adeno-associated virus serotype 9 (AAV9) vector construction and administration

AAV9 was used for overexpression of *Nfs1* gene *in vivo* with the use of the troponin T (cTnT) promoter to achieve cardiomyocyte-restricted gene targeting. AAV9-cTnT-Nfs1 and the negative control AAV9-cTnT-CTL were constructed by OBiO Technology Company (Shanghai, China). Mice were injected through the tail vein with AAV9-cTnT- *Nfs1* or AAV9-cTnT-CTL at the dose of 2 × 10^{11} vg/animal. Six weeks after the injection, heart samples were collected for assays.

2.7. Cell culture and RNA interference

Rat H9C2 cardiomyocytes were obtained from the ATCC. Cells were cultured in DMEM medium supplemented with 10 % FBS and cocktail of antibiotics. H9C2 cells grown to approximately 70 % confluence were transfected with control or YY1-siRNA, as described previously [31]. Specific siRNA molecules targeted to YY1 were synthesized by Gene Pharma Company (Shanghai, China). The siRNA sequences of the rat YY1 are: sense: 5′- CCUUCGACGGUUGUAAUAA-3′, antisense: 5′-UUAUUACAACCGUCGAAGG-3'. After 6-h transfection, cells were treated with or without 1 μM verteporfin for 48 h. After incubation, cells were harvested for analysis.

2.8. Iron measurement

Fe^{2+} and Fe^{3+} content in heart tissue were detected using commercial iron assay kit (Dojindo, Japan). Briefly, fresh mouse LV tissues were homogenized in PBS. After centrifugation, the supernatant was collected, and Fe^{2+} and Fe^{3+} levels were measured according to the manufacturer's instructions. Mitochondrial iron was also measured using MitoFerro-Green, which is a fluorescence probe designed for the detection of Fe^{2+} within mitochondria (Dojindo, Japan). Cells were incubated in 5 μM MFG solution for 30 min at 37 °C in the dark. Following washes with PBS, mitochondrial iron was observed using an Olympus FV3000 confocal microscopy.

2.9. Transmission electron microscopy and quantification

Transmission electron microscopy (EM) was applied to observe the ultrastructure of mouse LV tissues, as described previously [14]. In brief, fresh LV tissue blocks (1 mm^3) were immediately fixed in 2.5 % glutaraldehyde. The samples were dehydrated and embedded, and then ultrathin sections cut and stained. Finally, the samples were viewed in the transmission electron microscope (Hitachi Model H-7650) and images were acquired. Analysis of ultrastructural alterations of mitochondria was performed in images (magnification × 10,000) using Image Pro Plus 6.0 software.

2.10. Western blotting analysis

Total protein was prepared from LV tissues or NRVMs using RIPA lysis buffer. A nuclear protein extraction kit (Beyotime, Shanghai, China) was used for preparation of nuclear and cytoplasmic protein fractions from mouse LV tissues. Protein samples were separated on a sodium dodecyl sulfate-polyacrylamide gel and transferred to a polyvinylidene fluoride membrane, as described previously [31]. The membranes were initially incubated with primary antibodies (see Table S2) overnight (4 °C), and then with horseradish peroxidase-conjugated secondary antibodies (1:10000) for 1 h at room temperature. The bound antibodies were detected with an enhanced chemiluminescence detection system (Bio-Rad, USA) and quantified by densitometry using the ImageJ software.

2.11. Immunohistochemistry

LV tissues were fixed in formalin, embedded in paraffin, cut in sections (5 μm), and stained with Masson's trichrome reagent. Images were digitized (× 400 magnification) using a microscope (DP72; Olympus, Japan). The expression of NFS1 and 4-Hydroxynonenal (4-HNE) in the myocardium was determined using specific antibodies (1:200) and visualized with diaminobenzidine. Negative control was generated by incubating sections with anti-IgG antibody.

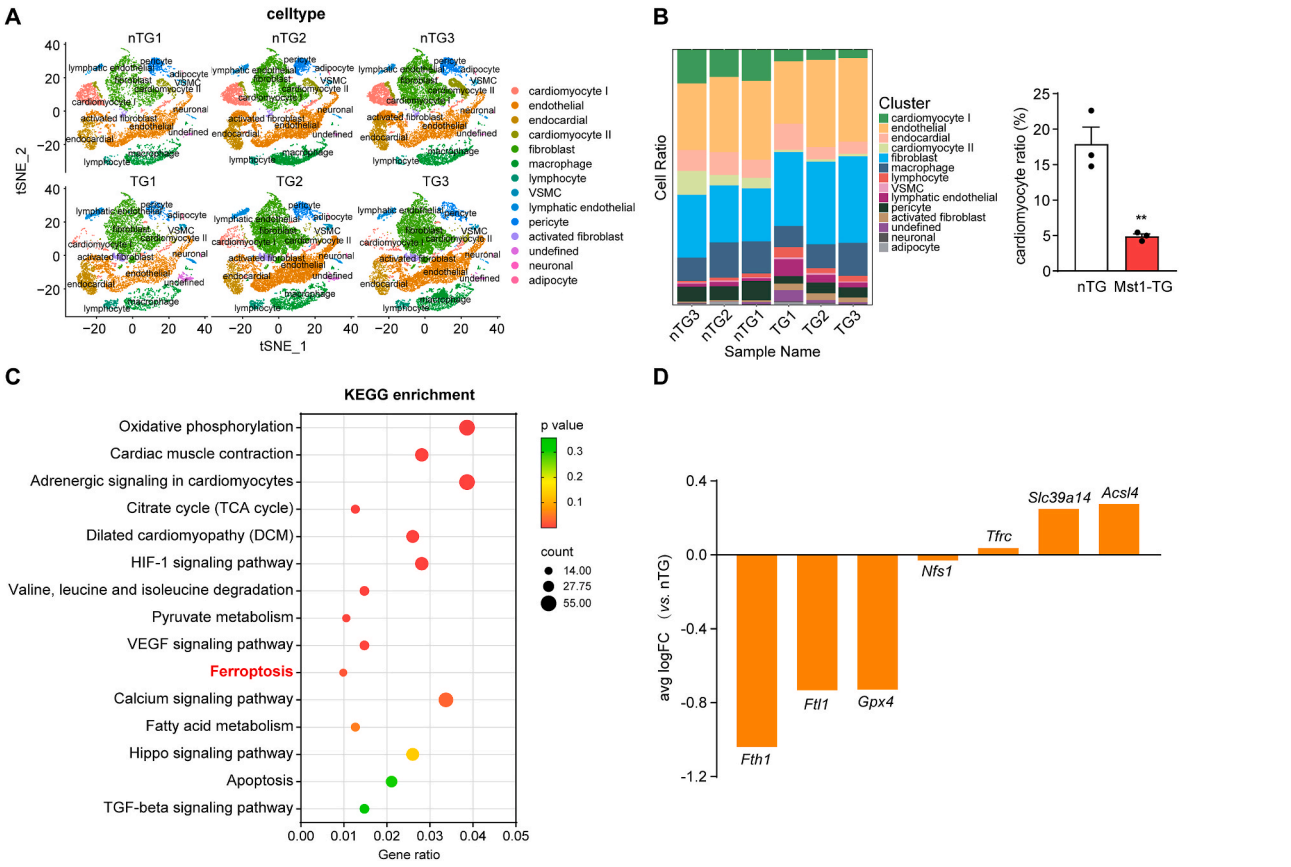

Fig. 1. Single-nucleus RNA-sequencing analysis of adult Mst1-TG mouse heart. ***A***. Representative tSNE plot showing differences in cell density among LV samples of nTG and TG mice (n = 3 each). ***B***. Cell-type composition of individual samples with colors representing different cell types. Cardiomyocyte ratio was calculated and presented as Mean ± SEM, $^{**}P < 0.01$ *vs.* nTG. ***C***. KEGG enrichment analysis for altered gene sets in Mst1-TG mouse cardiomyocytes relative to nTG. ***D***. Alterations in ferroptosis-related genes in cardiomyocytes from Mst1-TG relative to nTG group.

2.12. Immunofluorescent dual staining

Immunofluorescent dual-staining of LV sections was performed, as previously described [28]. In brief, formaldehyde fixed sections (5 μm) were incubated overnight at 4 °C with combination of rabbit anti-YAP antibody (1:200) and mouse anti-YY1 antibody (1:200). After incubation with appropriate fluorescence-labeled secondary antibodies (1 h, room temperature), the sections were finally incubated with DAPI for 10 min. Images were acquired with an Olympus FV3000 confocal microscopy.

2.13. Immunoprecipitation

Immunoprecipitation experiments were performed, as previously described [14]. In brief, nuclear protein was extracted from mouse LV tissues using the nuclear protein extraction kit (Beyotime, Shanghai, China). Cleared lysates were immunoprecipitated with anti-YAP1, anti-TEAD1 or anti-YY1 antibody, respectively, at 4 °C overnight, and then coupled to suspended protein A/G agrose beads (Santa Cruz, CA, USA). The beads were washed 3 times in 400 μL lysis buffer. Immunoprecipitates were boiled in SDS-Laemmli buffer and then analyzed by Western blotting using antibodies against YY1, TEAD1 or YAP1.

2.14. Cleavage under targets & Release using Nuclease (CUT&RUN) assay

The CUT&RUN was done using Assay Kit for qPCR (CST, #86652). H9C2 cells (1×10^5) or LV tissues (1 mg) were prepared, washed in 100 μL washing buffer, and incubated with ConA beads for 10 min (25 °C). Samples were then incubated overnight (4 °C) with antibodies against TEAD1, YY1or H3K27me3. pG-MNase enzyme was then added and the samples were incubated for 1 h (4 °C) followed by washing twice with DIG washing buffer. Then, the samples were incubated with $CaCl_2$ (10 mM) for 1 h (4 °C). After addition of 100 μL stop buffer, the samples were resuspended and incubated for 30 min (37 °C), then plated on a magnet and liquid was drained. After gentle washes with 80 % ethanol, DNA was eluted from the beads using double-distilled water. RT-qPCR tests were conducted in accordance with the manufacturer's recommendations.

2.15. Luciferase reporter assay

The *Nfs1*-promoter sequence was cloned onto the pGL4.1 vector. Cells were seeded into a 24-well plate at 40 % density, then transfected with 200 ng pGL4.1 plasmid and 4 ng pRL-TK-Renilla-luciferase plasmid. The transfected cells were collected 48 h later with Passive Lysis Buffer (Promega) according to the instructions. The subsequent steps were performed according to the protocol. The luciferase activity was measured by GloMax 20/20 luminometer (Promega). The relative luciferase activity was determined based on the ratio of firefly luciferase to Renilla luciferase.

2.16. Materials

Information of antibodies is provided in Table S2. Deferoxamine (DFO), Fer-1 and verteporfin were from MedChem Express (USA). Iron assay kit and MitoFerro-Green mitochondrial Fe^{2+} probe were products of Dojindo Laboratories (Japan). C11-BODIPY reagent was purchased

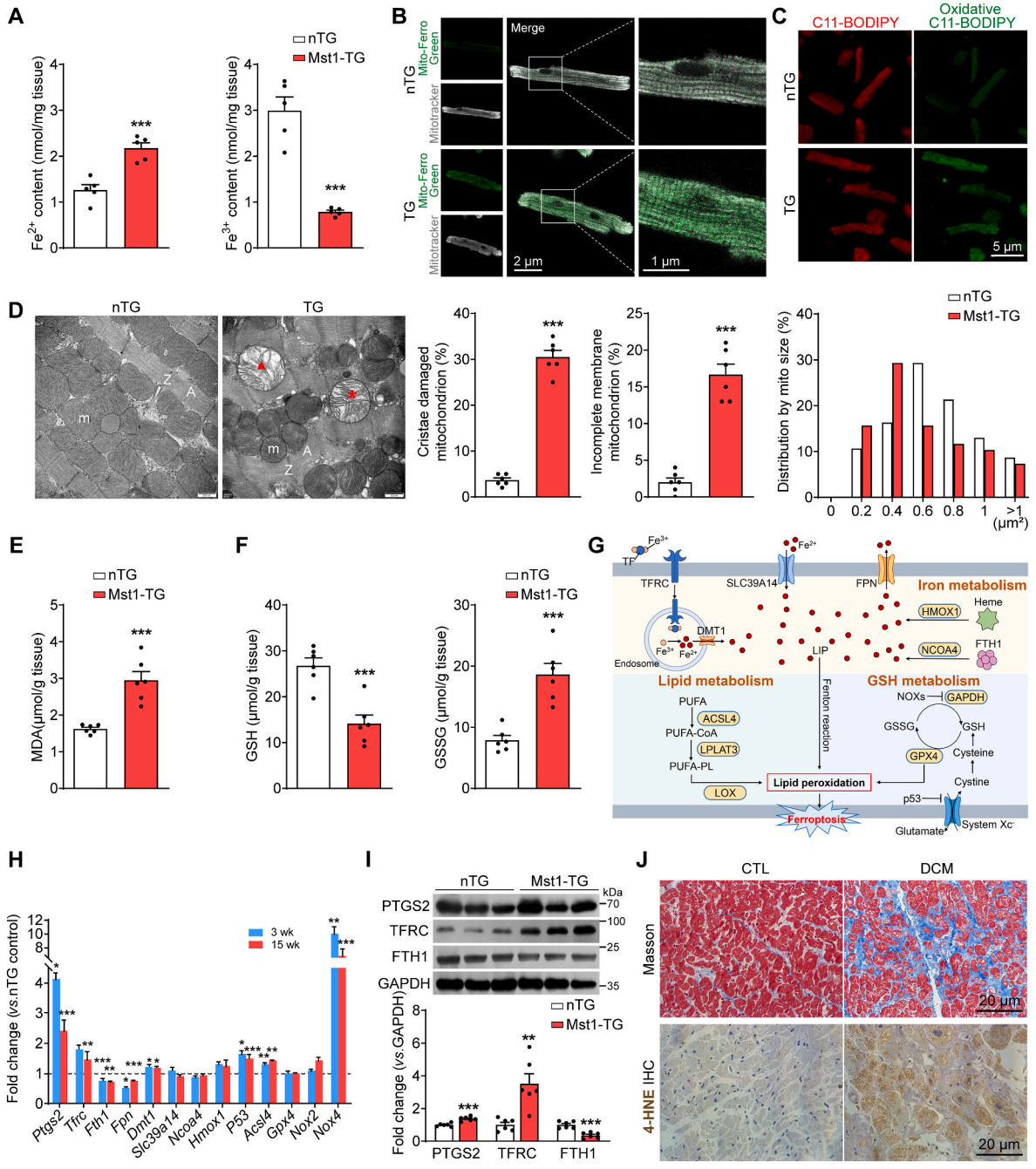

Fig. 2. Ferroptotic alterations in hearts of Mst1-TG mice or patients with dilated cardiomyopathy (DCM). ***A***: Labile Fe^{2+} and Fe^{3+} level in LV tissues (n = 5 per group). ***B***: Representative fluorescence imaging of mitochondrial Fe^{2+} using Mito-FerroGreen (green) in cardiomyocytes isolated from adult mouse hearts, mitochondria of cells were counterstained with Mitotracker (grey). ***C***: Representative fluorescence imaging of lipid peroxides (green, right panels) using C11-BODIPY in isolated cardiomyocytes from adult mouse hearts. ***D***: Electron micrographs showing mitochondria in LV tissues of adult nTG and Mst1-TG mice and quantitative analysis of damaged mitochondrion count and distribution of mitochondrial size (results from 500 to 800 measures per sample, n = 3 hearts per group, two batches of photos were acquired from 1 sample), magnification at 30,000. m: mitochondria; A: sarcomere A-band; Z: Z-line; *: mitochondria with disrupted cristae; ▲: mitochondria with incomplete outer-membrane. ***E***: level of MDA as a lipid peroxidation product in LV tissues. ***F***: GSH and GSSG level in LV tissues. ***G***: Schematic diagram summarizing the molecular and metabolic mechanisms involved in ferroptosis. ***H***: Expression of individual ferroptosis related genes. Data were from RNA-seq of 3-wk or 15-wk nTG and Mst1-TG mice. ***I***: Western blotting images and mean values of ferroptotic marker proteins in the LV. ***J***: Masson trichrome staining or immunohistochemistry staining of lipid peroxidative product 4-Hydroxy-2-Nonenal (4-HNE) in sections of LV tissues from heart disease-free control subjects (CTL) or DCM patients. Data are presented as Mean ± SEM, n = 6, $^{*}P < 0.05$, $^{**}P < 0.01$, $^{***}P < 0.001$ *vs.* nTG.

from Thermo Fisher Scientific Inc. DHE and mitotracker reagents and GSH assay kit were purchased from Beyotime Institute of Biotechnology (Shanghai, China). MDA and ATP assay kits were obtained from Jiancheng Bioengineering Institute (Nanjing, China). Assay kits for cTnI and lactate were from Elabscience Biotechnology Co. Ltd (Wuhan, China).

2.17. Statistical analysis

All data were presented as mean ± SEM. Results were analyzed using GraphPad Prism 9 software. Statistical comparisons among more than two groups were performed by one-way analysis of variance (ANOVA) with Bonferroni's *post-hoc* test. A Student's *t*-test was used to compare

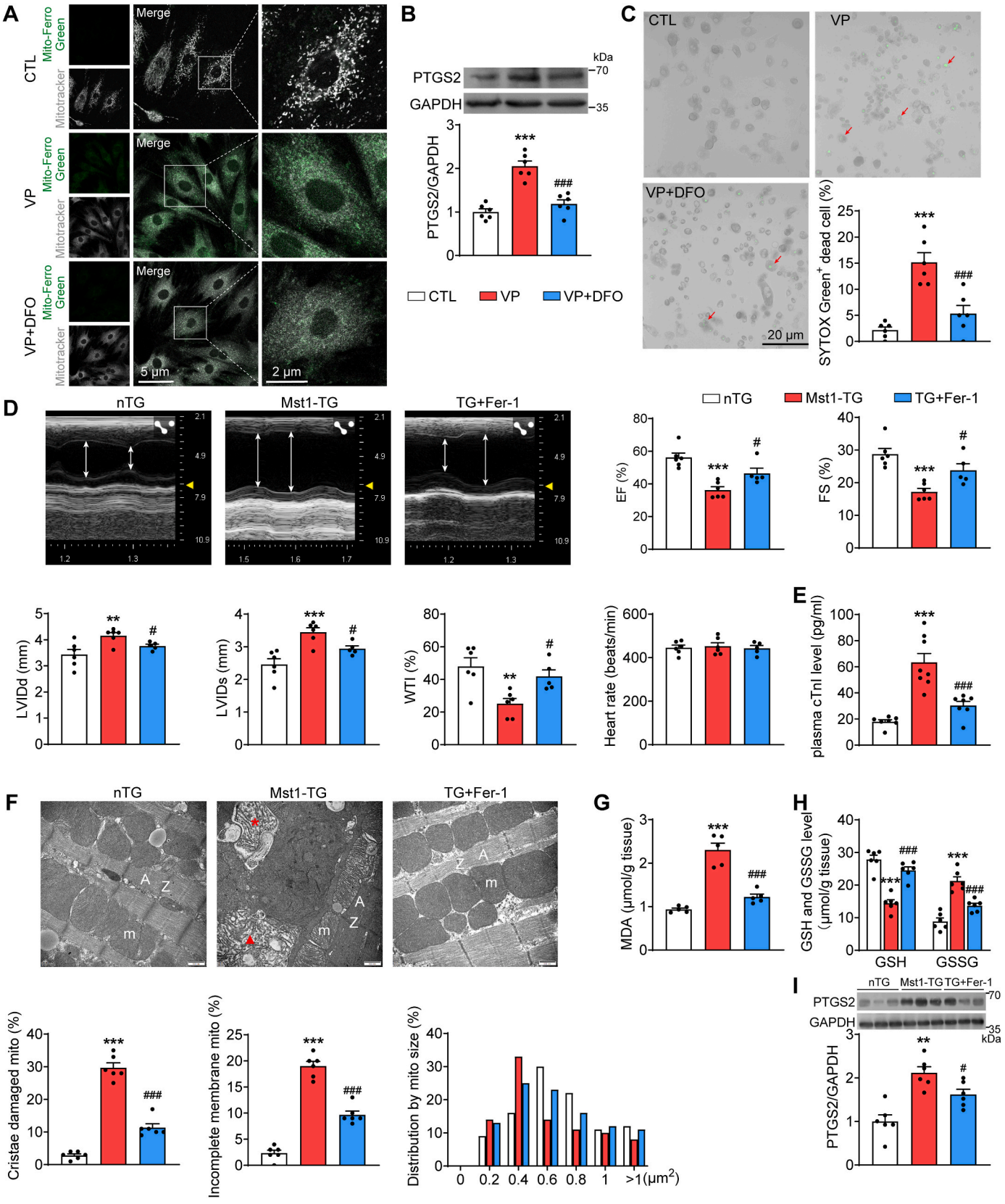

(caption on next page)

Fig. 3. Effects of deferoxamine (DFO) and ferrostatin-1 (Fer-1) on cardiomyocyte ferroptosis induced by Hippo pathway activation (Mst1-TG) or YAP inactivation. In panels A–C, neonatal rat ventricular cardiomyocytes (NRVMs) were treated with or without YAP inhibitor verteporfin (VP, 1 μM) or iron chelator DFO (100 μM) for 48 h. ***A***: Representative Mito-FerroGreen and Mitotracker fluorescence imaging for mitochondrial Fe^{2+}. ***B***: Western blotting images and mean values of PTGS2 in NRVMs. ***C***: NRVM images and quantitative analysis of SYTOX Green dead cell (red arrows). n = 6 dishes per group, $^{***}P < 0.001$ *vs.* CTL; $^{\#\#\#}P < 0.001$ *vs.* VP. Panel D–I contain data from adult mice administrated with Fer-1 (1 mg/kg, once every second day, i.p.) or solvent for 4 weeks. ***D***: Representative M-mode tracings from short-axis LV 2-D images and echocardiography derived ejection fraction (EF), fractional shortening (FS), LV internal diameters at end-diastole (LVIDd) and end-systole (LVIDs), wall thickening index (WTI) and heart rate. ***E***: Plasma levels of cTnI. ***F***: Electron micrographs showing mitochondria in LV tissues and quantitative analysis of damaged mitochondrion count and distribution of mitochondrial size (n = 3 hearts per group, two batches of photos were acquired from 1 sample), magnification at 30,000. m: mitochondria; A: A-band; Z: Z-line; *: mitochondria with disrupted cristae; ▲: mitochondria with incomplete outer-membrane. ***G***: MDA level in LV tissues. ***H***: GSH and GSSG level in LV tissues. ***I***: Western blotting images and mean values of PTGS2 in the LV. Data are presented as Mean ± SEM, n = 6, $^{*}P < 0.05$, $^{**}P < 0.01$, $^{***}P < 0.001$ *vs.* nTG; $^{\#}P < 0.05$, $^{\#\#\#}P < 0.001$ *vs.* Mst1-TG.

differences between only two groups. Nonparametric test was used to analyze differences among groups of EM-derived parameters that were not normally distributed. Statistical comparisons between two groups were performed by the Mann-Whitney *U* test, and the Kruskal-Wallis test followed by the Dunn's multiple comparison test for among more than two groups. A value of $P < 0.05$ was considered to be significantly different.

3. Results

3.1. SnRNA-seq revealed cardiomyocyte loss and ferroptosis in Mst1-TG mouse heart

We performed snRNA-seq on LV samples from adult nTG and Mst1-TG mice. After demultiplexing and mapping to mouse reference genome, 13 major cell types were annotated using cell type-specific gene markers, including two clusters of cardiomyocytes (cardiomyocyte I and II). tSNE representation of isolated nuclei showed cardiomyocyte density was lower in TG mouse LVs relative to nTG controls (Fig. 1A). Composition analysis indicated that the averaged cell ratio of cardiomyocytes of both clusters was significantly reduced in Mst1-TG compared with nTG hearts (average 4.9 % vs. 17.9 %, Fig. 1B). KEGG enrichment analysis in cardiomyocytes confirmed differentially expressed genes (DEGs) in Mst1-TG mouse hearts mainly enriched in categories of mitochondrial metabolism, cardiomyopathy and ferroptosis. Notably, alterations in the ferroptosis pathway were significant whereas that in the apoptosis pathway were insignificant (Fig. 1C). Expression of ferroptosis-related genes in cardiomyocytes was further analyzed. In TG cardiomyocytes, iron import genes *Tfrc* and *Slc39a14* and lipid peroxidation related gene *Acsl4* were upregulated, whilst iron storage genes *Fth1* and *Ftl1*, anti-oxidation gene *Gpx4* and ISC assembling involved gene *Nfs1* were downregulated (Fig. 1D). Accordingly, cardiomyocyte loss represents a key mechanism for the onset of DCM in the Mst1-TG model.

3.2. Ferroptosis-associated alterations in the myocardium of Mst1-TG mice or DCM patients

To confirm existence of cardiomyocyte ferroptosis in Mst1-TG mice with established DCM, we examined several ferroptosis markers. Relative to nTG values, the labile Fe^{2+} level of LV tissues doubled while the total free Fe^{3+} level decreased by 70 % in Mst1-TG group (Fig. 2A). By preparing cardiomyocytes from adult mouse hearts and staining mitochondrial Fe^{2+} using a mitochondrial Fe^{2+} probe Mito-FerroGreen, we found that the increased Fe^{2+} level was mainly limited to mitochondria of cardiomyocytes of Mst1-TG mice (Fig. 2B). In addition, the C11-BODIPY staining of cardiomyocytes showed that whilst the total lipid content (red color) was unchanged, peroxidative lipid content (green color) significantly increased in cardiomyocytes of Mst1-TG relative to nTG group (Fig. 2C).

We found evident abnormalities of mitochondrial ultra-structure implicating ferroptosis in Mst1-TG hearts. Relative to nTG controls, EM images revealed alterations including shrunken mitochondria, increased density of outer membrane, mitochondria with incomplete outer membrane, and severe damage to cristae (Fig. 2D). The level of MDA, representing a lipid peroxidation product, was increased in the Mst1-TG myocardium (Fig. 2E). Furthermore, myocardial content of antioxidative GSH was reduced by 50 % while that of oxidized glutathione (GSSG) doubled in Mst1-TG versus nTG hearts (Fig. 2F).

Multiple molecular and metabolic mechanisms are implicated in ferroptosis including excessive free Fe^{2+} accumulation, lipid peroxidation and GSH deficiency (Fig. 2G) [6]. We further explored changes in the expression of ferroptosis-related genes by analyzing RNA-seq database that we previously obtained from young (3-week) and adult (15-week) Mst1-TG and nTG hearts (GSE106201) [10]. In LV tissues from Mst1-TG mice at both ages studied, there was 2- to 4-fold increase in *Ptgs2* as a ferroptosis marker gene. Upregulated genes also included cell death-related gene *p53* and iron import genes *Tfrc* and *Dmt1*, whilst expression of *Fth1* and *Fpn* encoding iron storage and export proteins was downregulated. These alterations, i.e. upregulated iron import genes together with downregulated iron storage and export genes, indicate augmentation of the iron-starvation-response that underlies the elevated Fe^{2+} level in the Mst1-TG myocardium (Fig. 2A). In addition, *Acsl4* and *Nox4* are genes participated in lipid peroxidation, and their expression was markedly upregulated in Mst1-TG hearts (Fig. 2H). These transcriptomic findings were verified by Western blotting showing increased protein abundance of PTGS2 and TFRC, and reduced level of FTH1 protein in adult Mst1-TG myocardium (Fig. 2I). Collectively, these findings indicate the occurrence of cardiomyocyte ferroptosis in the Mst1-TG model with cardiac Hippo pathway activation and cardiomyopathy.

Using the myocardial samples from patients with DCM and heart disease-free control subjects, we investigated changes that might imply ferroptosis of cardiomyocytes. By histology, extensive collagen deposition, loss of cardiomyocytes and increased level of 4-HNE as a lipid peroxidation product were evident in the myocardium of DCM patients relatively to controls (Fig. 2J).

3.3. Treatment with iron chelator or antioxidant attenuated ferroptosis induced by hippo pathway activation and YAP inactivation

Using NRVMs in culture treated with verteporfin (VP, a YAP-TEAD1 inhibitor) or Mst1-TG mice, we then tested effects of the iron chelator DFO or the ferroptosis inhibitor Fer-1 on cardiomyocyte ferroptosis. In cultured NRVMs, incubation with VP (1 μM) for 48 h significantly increased mitochondrial Fe^{2+} content, protein expression of PTGS2 and peroxidative lipid level (Fig. 3A and B and Fig. S1). SYTOX Green probe revealed that treatment with VP led to a 6-fold increase in cell death relative to untreated cells (Fig. 3C). In contrast, treatment of NRVMs with DFO (100 μM) for 48 h effectively reduced mitochondrial Fe^{2+} content and attenuated VP-induced lipid peroxidation and ferroptosis. Thus, YAP-TEAD1 inhibition in cardiomyocytes upregulated mitochondrial Fe^{2+} level and induced ferroptosis.

In Mst1-TG mice, a 4-week period of treatment with a lipid peroxidation antioxidant Fer-1 significantly improved LV systolic function measured as EF, FS and WTI, and limited LV enlargement without change in the heart rate level compared with untreated TG mice (Fig. 3D). Effectiveness of Fer-1 treatment was also reflected by

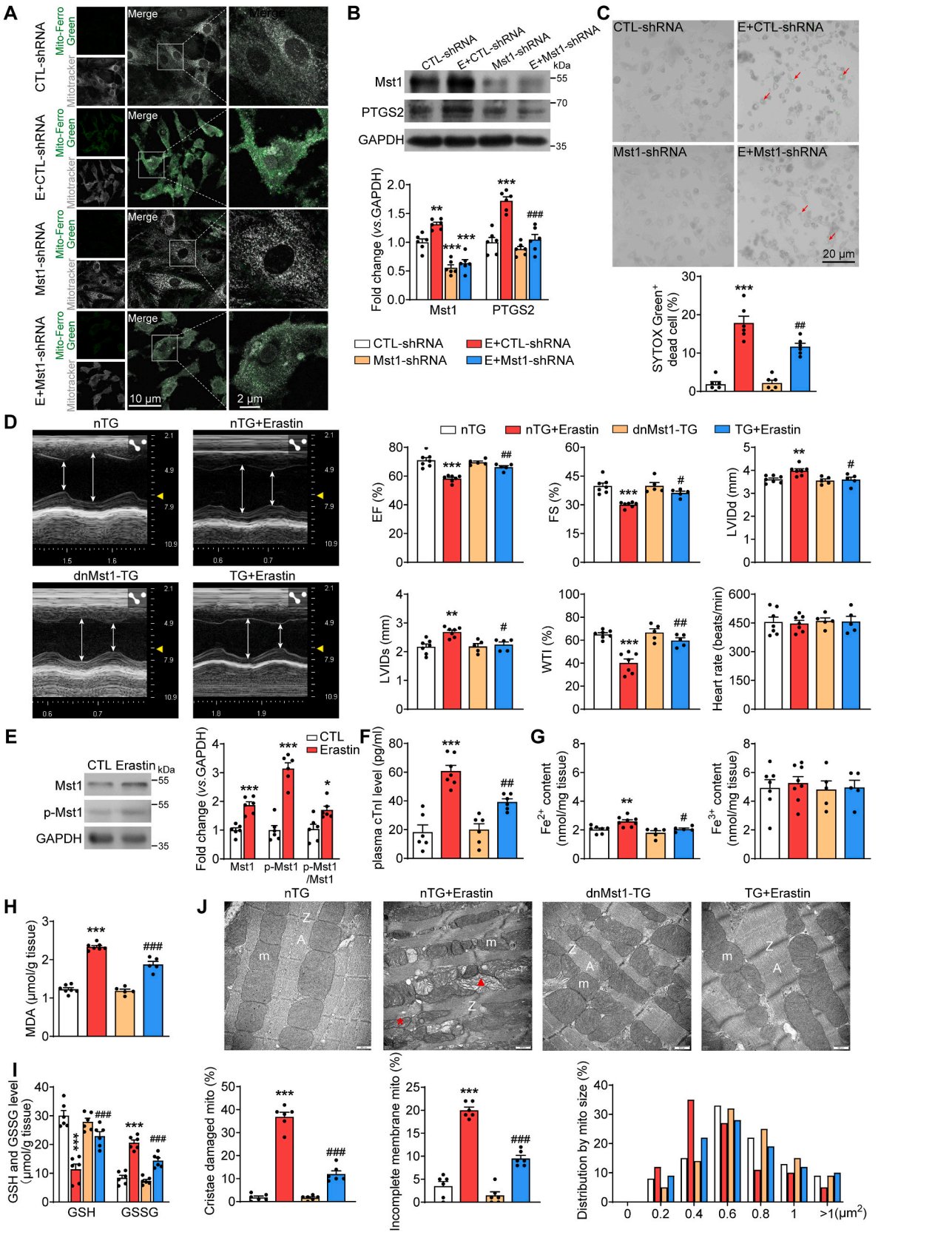

(caption on next page)

Fig. 4. Effect of Hippo pathway inactivation on erastin-induced cardiomyocyte ferroptosis. In panels A–C, NRVMs were infected for 24 h with adenovirus carried control shRNA (CTL-shRNA) or Mst1-shRNA, and cells were then treated with erastin (E, 0.1 μM, 24 h) or vehicle. ***A***: Representative Mito-FerroGreen and Mitotracker fluorescence imaging for mitochondrial Fe^{2+}. ***B***: Western blotting images and mean values of Mst1 and PTGS2 in NRVMs. ***C***: Images and quantitative analysis of SYTOX Green stained dead cells (red arrows). n = 6 dishes/group, $^{***}P < 0.001$ *vs.* CTL-shRNA; $^{\#}P < 0.05$, $^{\#\#}P < 0.01$, $^{\#\#\#}P < 0.001$ *vs.* E + CTL-shRNA. Data in panels D–I were from adult nTG and dnMst1-TG mice treated for 4 weeks with erastin (20 mg/kg, i.p., 3 times per week) or vehicle. ***D***: Representative M-mode tracings from short-axis LV 2-D echocardiographic images. EF, FS, LVIDd, LVIDs, WTI and heart rate were derived from LV M-mode tracings. ***E***: Western blotting images and mean values for Mst1 and Mst1 phosphorylation at Thr183 site in LV tissues of healthy wild-type mice with or without erastin treatment. n = 6/group, $^{*}P < 0.05$, $^{***}P < 0.001$ *vs.* CTL. ***F***: Plasma levels of cTnI. ***G***: Labile Fe^{2+} and Fe^{3+} levels in LV tissues. ***H***: MDA level in LV tissues. ***I***: GSH and GSSG level in LV tissues. ***J***: Electron micrographs showing mitochondria in LV tissues and quantitative analysis of damaged mitochondrion count and distribution of mitochondrial size (n = 3 hearts per group, two batches of photos were acquired from 1 sample), magnification at 30,000. m: mitochondria; A: A = band; Z: Z = line; *: mitochondria with disrupted cristae; ▲: mitochondria with incomplete outer-membrane. $^{*}P < 0.05$, $^{**}P < 0.01$, $^{***}P < 0.001$ *vs.* nTG; $^{\#}P < 0.05$, $^{\#\#}P < 0.01$, $^{\#\#\#}P < 0.001$ *vs.* nTG + Erastin. Data are presented as Mean ± SEM.

significant reductions in plasma level of cTnI, myocardial levels of MDA and GSSG, and myocardial PTGS2 protein in Mst1-TG mice (Fig. 3E, G, 3H and 3I). Other features of ferroptotic cardiomyocytes, including changes in GSH level and abnormal mitochondrial ultrastructure, were also ameliorated by Fer-1 treatment (Fig. 3H and F).

3.4. *Mst1 inactivation mitigated erastin-induced cardiomyocyte ferroptosis*

The regulatory effect of Hippo pathway on cardiomyocyte ferroptosis was investigated *in vitro* (NRVMs in culture) and *in vivo* (dnMst1-TG mice) with ferroptosis induced by treatment with erastin. In NRVMs, erastin (0.1 μM, 24 h) induced cell ferroptosis measured by elevated levels of mitochondrial Fe^{2+}, PTGS2 protein, lipid peroxidation and cell death (Fig. 4A–C and S2). Treatment with Ad-Mst1-shRNA in NRVMs reduced Mst1 expression by approximately 60 %, lowered mitochondrial level of Fe^{2+}, and suppressed PTGS2 protein abundance or lipid peroxidation, and inhibited cell death by about 30 % (Fig. 4A–C, Fig. S2).

dnMst1-TG is a model of cardiomyocyte Mst1 inactivation by overexpressing the kinase-dead mutant Mst1 gene [25]. Erastin was administered to nTG and dnMst1-TG mice for 4 weeks. In nTG mice, treatment with erastin induced LV dilatation and reduction in EF, FS and WTI (Fig. 4D). Erastin treatment also increased plasma level of cTnI or myocardial contents of Fe^{2+}, MDA and GSSG, and reduced myocardial GSH content (Fig. 4F–I). In erastin-treated nTG mice, there was increased myocardial protein expression of Mst1 and its Thr183-phosphorylation (Fig. 4E), mitochondrial ferroptotic changes with increased fractions of damaged and shrunken mitochondria (Fig. 4I). Importantly, erastin-induced alterations in these ferroptosis-specific markers, as seen in nTG mice, were all attenuated in the dnMst1-TG mice (Fig. 4F–I).

3.5. *Pivotal role of NFS1 downregulation in ferroptosis induced by hippo pathway activation*

ISC biosynthesis is the important iron metabolic pathway in mitochondria and plays a key role in cellular biological function (Fig. 5A). We further analyzed the RNA-seq data from 3- and 15-week-old mouse hearts to identify whether Hippo pathway activation altered key molecules participating in the ISC biosynthesis. Notably, majority of genes related to the ISC biosynthesis were downregulated, especially ISC assembling genes like *Nfs1*, *Fxn* and *Iscu* (Fig. 5B). ISC deficiency is known to evoke the iron-starvation-response through ISC-unbound aconitase that translocates into the nucleus and, as an iron regulatory protein (IRP), upregulates TFRC while downregulates FTH1, leading to cellular iron overload (Fig. 5C). Expression of these proteins was further examined by Western blotting. We found upregulated IRP1 expression in the whole cell or the nucleus (Fig. 5D and E) but downregulated NFS1 expression in LV tissues of Mst1-TG relative to nTG group (Fig. 5D). Using RNA-seq data of human DCM and non-heart disease control heart samples [32], we explored the expression of ISC biosynthesis related genes. Whereas there were diverse changes in this gene set in human DCM myocardium compared with that in Mst1-TG hearts, *NFS1* mRNA was similarly downregulated in both settings (Fig. 5F). Immunohistochemistry of LV sections of human DCM hearts revealed a 45 % downregulation of NFS1 protein expression (Fig. 5G).

Considering a central role of NFS1 in mitochondrial iron homeostasis, we then studied the role of NFS1 in mitochondrial iron metabolism and cardiomyocyte ferroptosis in cultured NRVMs with NFS1 knockdown. Transfection with Ad-NFS1-shRNA induced NFS1 knockdown by about 50 %, which was associated with significantly elevated mitochondrial Fe^{2+} content, 6-fold increase in cell death fraction, and elevated protein expression of PTGS2 and IRP1, whilst expression of FTH1 was reduced (Fig. 5H–J). Furthermore, treatment with erastin (0.1 μM, 24 h) in NRVMs downregulated both NFS1 and FTH1, but upregulated IRP1. Once again, these effects of erastin were alleviated by Mst1 knockdown (Fig. 5K). Similarly, the degree of erastin-induced downregulation of NFS1 and FTH1, but upregulation of PTGS2 and IRP1, seen in the LV tissues of erastin-treated nTG mice, were all attenuated in dnMst1-TG mice (Fig. 5L). These results demonstrated that Hippo pathway activation in cardiomyocytes induced ferroptosis via downregulating NFS1.

3.6. *Activation of hippo pathway downregulated NFS1 expression by inducing imbalanced YAP-YY1 and YAP-TEAD1 signaling in cardiomyocytes*

We further studied the mechanism responsible for NFS1 downregulation by Hippo pathway activation. We analyzed the mouse *Nfs1* promoter motifs using the JARSPAR database and UCSC Genome Browser and predicted both TEAD1 and YY1 as potential transcriptional factors that bind to the *Nfs1* promoter (Fig. 6A and B). Fig. 6C shows the binding regions of TEAD1 and YY1 in the *Nfs1* promoter tested by qPCR. In cultured H9C2 cells, CUT&RUN and RT-qPCR assays revealed that both TEAD1 and YY1 could bind to the *Nfs1* promoter. Inhibition of YAP-TEAD1 using VP (1 μM, 48 h) reduced the binding by TEAD1, which was accompanied by a concomitant increase in YY1 binding to the *Nfs1* promoter (Fig. 6D). By dual-luciferase promoter activity analysis, we found that inhibition of YAP-TEAD1 with VP reduced the transcriptional activity of *Nfs1* promoter, indicating transcriptional activation of *Nfs1* by YAP-TEAD1 binding. Moreover, the inhibition of *Nfs1* expression by VP was reversed by YY1 knockdown using YY1-siRNA, suggesting that with TEAD1 inhibition, YY1 binds to the *Nfs1* promoter and suppresses *Nfs1* transcription (Fig. 6E). Similarly, Western blotting showed that VP suppressed NFS1 expression whilst in the presence of VP, YY1-siRNA effectively restored NFS1 expression (Fig. 6F). Thus, these findings implicate that TEAD1 activates but YY1 suppresses *Nfs1* expression.

In Mst1-TG mouse LV tissues, CUT&RUN and RT-qPCR assays showed reduced TEAD1 but increased YY1 enrichment, together with higher H3K27me3 abundance at the *Nfs1* promoter (Fig. 6G). By immunoblotting, we found that the expression level of both Src and total YAP increased in the myocardium of Mst1-TG mice. To assess alterations of YAP, TEAD1 and YY1 in the cytoplasm and nuclei, we prepared cytoplasmic and nuclear protein fractions of mouse LV tissues for

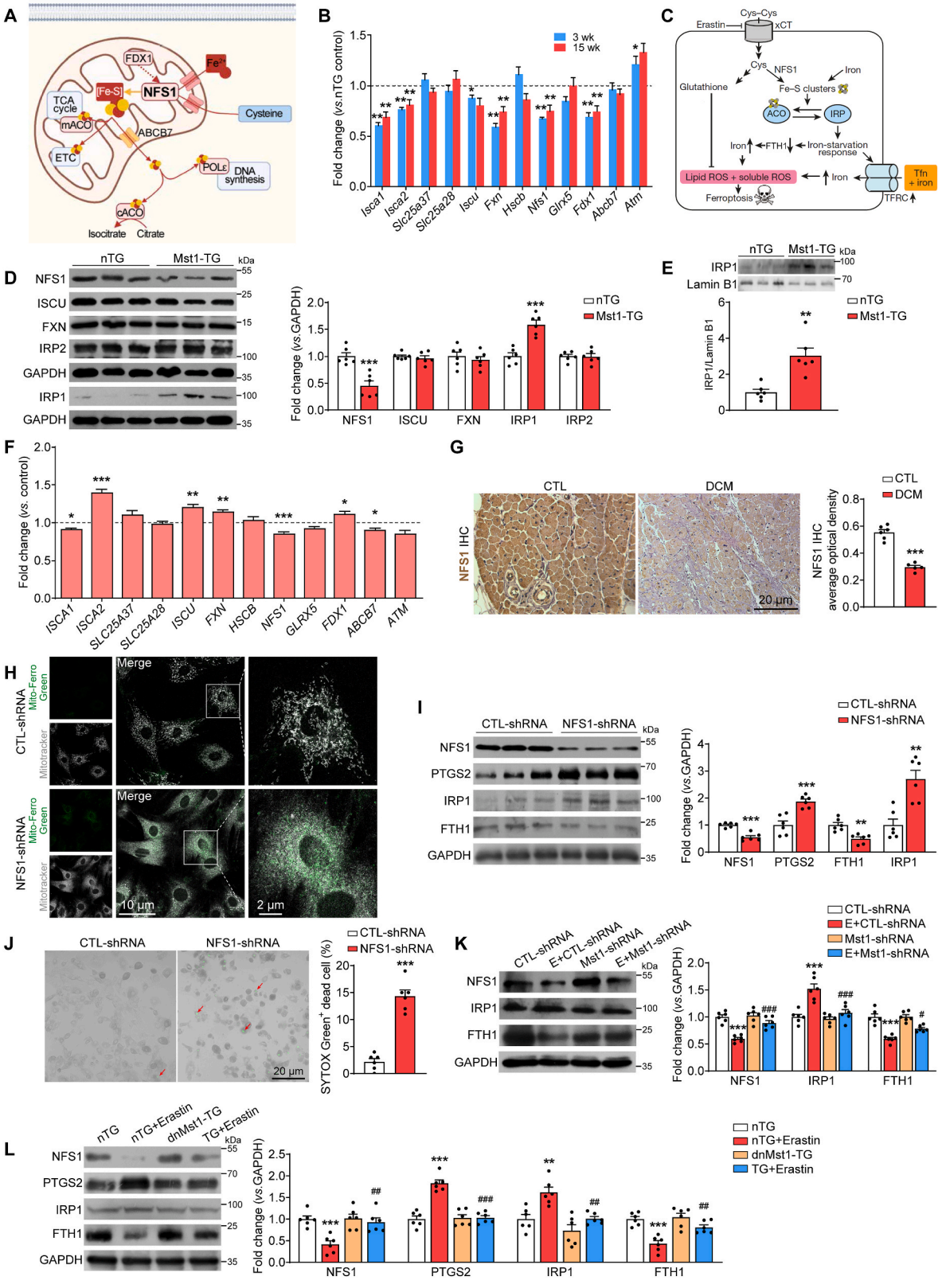

(caption on next page)

Fig. 5. Role of NFS1 in cardiomyocyte ferroptosis induced by Hippo pathway activation *in vivo* and *in vitro*. ***A***: Schematic diagram summarizing the role of NFS1 and iron-sulfur cluster (ISC) containing enzymes. ***B***: Expression of genes involved in ISC biosynthesis based on RNA-seq data of LV tissues from 3- and 15-wk nTG and Mst1-TG mice. ***C***: Schematic of the proposed model by which NFS1 suppression results in loss of ISCs, that sequentially evokes the iron-starvation-response. ***D*** and ***E***: Western blotting images and mean values for marker proteins of ferroptosis and ISC biosynthesis and nuclear IRP1 in LV tissues. ***F***: Expression in LV tissues of individual genes involved in ISC biosynthesis. Data were obtained from NCBI GEO database (GSE116250) of heart disease-free control subjects (n = 14) and DCM patients (n = 37) [29]. ***G***: Images and quantitative analysis of NFS1 immunohistochemistry staining in sections of LV tissues from control and DCM patients, control n = 6, DCM n = 5. $^{*}P < 0.05$, $^{**}P < 0.01$, $^{***}P < 0.001$ *vs.* nTG or control. Panel H–J: NRVMs were infected with adenovirus carried CTL-shRNA or NFS1-shRNA for 48 h. ***H***: Representative Mito-FerroGreen and Mitotracker fluorescence imaging for mitochondrial Fe^{2+}. ***I***: Western blotting images and mean values for marker proteins of ferroptosis and ISC biosynthesis in NRVMs. ***J***: Images and quantitative analysis of SYTOX Green stained dead cells (red arrows). n = 6 dishes/group, $^{**}P < 0.01$, $^{***}P < 0.001$ *vs.* CTL-shRNA. ***K*** and ***L***: Western blotting images and mean values for proteins involving in ferroptosis and ISC biosynthesis in NRVMs with different treatment, or in erastin-treated nTG and dnMst1-TG mouse hearts. n = 6/group, $^{**}P < 0.01$, $^{***}P < 0.001$ *vs.* CTL-shRNA or nTG; $^{\#\#}P < 0.01$, $^{\#\#\#}P < 0.001$ *vs.* E + CTL-shRNA or nTG + Erastin. Data are presented as Mean ± SEM.

Western blotting, and found higher nuclear abundance of YY1, YAP and Y357-pYAP, but lower abundance of TEAD1. In the cytoplasmic protein fraction, abundance of YAP and S127-pYAP was increased, yielding a higher ratio of cytoplasmic YAP to nuclear YAP in LVs of Mst1-TG relative to nTG group (Fig. 6H). By Co-IP experiment, nuclear interaction of YAP-YY1 enhanced, whilst that of YAP-TEAD1 reduced in Mst1-TG relative to nTG hearts (Fig. 6I). We also analyzed RNA-seq data of myocardial samples from human patients with DCM, and found that gene expression of TEAD1 was significantly suppressed (Fig. S3). This finding was supported by dual-immunofluorescence imaging analysis revealing an enhanced nuclear interaction of YAP-YY1 in the myocardium from Mst1-TG mice or from DCM patients relative to respective controls (Fig. 6J). These data demonstrated that Hippo pathway activation increased the enrichment of YAP-YY1 to *Nfs1* promoter whilst reduced the enrichment of YAP-TEAD1. Such opposite changes are responsible for histone hypermethylation at the *Nfs1* promoter that underlies the NFS1 downregulation.

3.7. *NFS1 overexpression mitigated cardiomyocyte ferroptosis and LV dysfunction in Mst1-TG mice*

To evaluate the effect of maintenance of cardiomyocyte NFS1 expression, we constructed Ad-NFS1 virus for viral transfection of *Nfs1* gene in cultured NRVMs, or AAV9-cTnT-NFS1 for *in vivo* testing in Mst1-TG mice. In NRVMs treated with erastin, infection with Ad-NFS1 virus almost doubled NFS1 protein expression and effectively mitigated both elevation of mitochondrial Fe^{2+} content and cell death fraction. The expression of PTGS2, IRP1 and FTH1 was also restored by Ad-NFS1 virus treatment (Fig. 7A–C).

We then tested the effect of AAV9-cTnT-NFS1 in Mst1-TG mice by intravenous administration of AAV9-cTnT-NFS1 or control virus. Viral infection efficacy was confirmed by the fluorescence intensity of it conjugated GdGreen in myocardial sections (Fig. S4). At week-6 after the injection, AAV9-cTnT-NFS1 treated mice showed a 1.29-fold increase in the myocardial NFS1 expression (Fig. 7I). Importantly, virally mediated NFS1 expression in cardiomyocyte was associated with significant improvement of LV function in Mst1-TG mice, indicated by the increment of EF, FS and WTI, and reduction in LVIDd and LVIDs relative to Mst1-TG mice received control virus (Fig. 7D). Importantly, virally mediated cardiomyocyte NFS1 expression in Mst1-TG mouse myocardium significantly reversed alterations in ferroptotic markers, including higher levels of plasma cTnI, myocardial levels of Fe^{2+}, MDA and GSSG, and decreased myocardial contents of Fe^{3+} and GSH (Fig. 7E–H). Likewise, AAV9-mediated NFS1 expression largely abolished upregulation of PTGS2 (Fig. 7I) and IRP1 (either in whole tissue or nuclear samples, Fig. 7I and J), or repression of FTH1 (Fig. 7I).

3.8. *Restoring NFS1 expression improved myocardial mitochondrial function in Mst1-TG model*

With these encouraging findings, we elected to examine *in vivo* the effect of AAV9-mediated NFS1 expression on cardiomyocyte mitochondrial function in Mst1-TG mice. Animal were injected with AAV9-CTL or AAV9-NFS1 virus and studied 6 weeks after the injection. Myocardial content of ATP was significantly lower whilst tissue and plasma levels of lactate were higher in AAV9-CTL group, and these changes were largely normalized by the treatment with AAV9-NFS1 virus (Fig. 8A and B). We measured the activity of ISC binding protein aconitase as an indicator for ISC bioavailability. Control Mst1-TG hearts exhibited suppressed aconitase activity, which was largely reversed by the treatment with AAV9-NFS1 virus (Fig. 8C). We also obtained evidence for beneficial effects by the maintenance of NFS1 expression on ultrastructure of mitochondria. EM images of LV tissues of TG mice revealed that treatment with AAV9-NFS1 virus ameliorated abnormalities of mitochondrial ultrastructure associated with ferroptosis, in particular percentages of damaged and shrunken mitochondria (Fig. 8D). We determined changes in oxidative stress level in Mst1-TG myocardium. In Mst1-TG mice treated with the control AAV9 virus, DHE staining showed elevated O_2^- level, and this was largely abolished by treatment with AAV9-NFS1 virus (Fig. 8E). Collectively, maintenance of cardiomyocyte NFS1 expression in Mst1-TG mice alleviated cardiomyocyte ferroptosis, mitochondrial dysfunction and cardiomyopathy.

4. Discussion

A few novel findings have been made in the current study. *First*, we provide evidence for a causal link between Hippo pathway activation and cardiomyocyte ferroptosis, which contributes to the initiation and development of cardiomyopathy. *Second*, mechanistically, activation of Hippo pathway in cardiomyocytes promotes nuclear YAP-YY1 interaction and binding to the *Nfs1* promoter, together with reduced YAP-TEAD1 binding, resulting in downregulated expression of NFS1. Loss of NFS1 activity interferes with ISC biosynthesis and augments the iron-starvation-response, leading to mitochondrial Fe^{2+} overload and ferroptosis. *Third*, inhibition of ferroptosis or virally mediated maintenance of NFS1 expression in cardiomyocytes mitigates mitochondrial dysfunction and DCM phenotypes in Mst1-TG mice.

Significant loss of cardiomyocytes in the setting of DCM is evident by our snRNA-sequencing in the Mst1-TG hearts and by histological analysis of heart samples from DCM patients, consistently showing cardiomyocyte loss and lipid peroxidation. Accumulating studies have defined molecular and metabolic features associated with ferroptosis, including iron overload, lipid peroxidation and defect in the metabolism of antioxidant GSH [19]. In the present study, we determined multiple ferroptosis-associated changes in heart tissues or cultured cells to confirm the occurrence of cardiomyocyte ferroptosis. These markers included labile Fe^{2+} and Fe^{3+} contents as well as mitochondrial Fe^{2+} level by using the Mito-FerroGreen probe, GSH and GSSG levels, ROS levels, lipid peroxidation by assaying MDA, oxidative lipids by 4-HNE as lipid peroxidation products or by C11-BODIPY probe. Ferroptosis-related ultrastructural changes of mitochondrion were also analyzed using EM images. In addition, we determined gene profiles and protein levels of markers of ferroptosis, iron metabolism, lipid peroxidation and GSH metabolism.

Earlier study in the Mst1-TG model reported cardiomyocyte

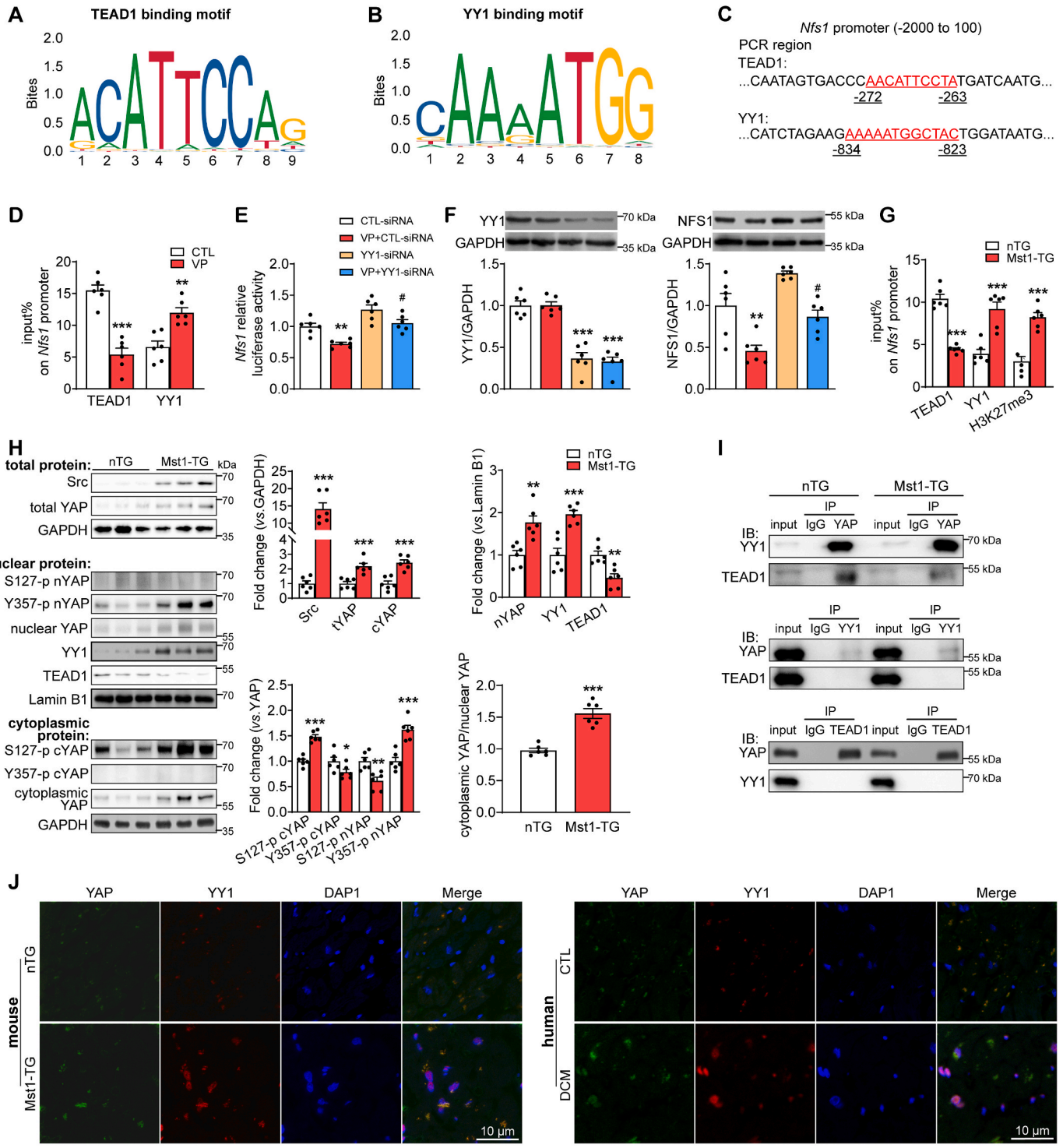

Fig. 6. Altered regulation of NFS1 expression upon Hippo pathway activation. ***A*** and ***B***: The consensus mouse TEAD1 and YY1 binding motifs predicted from JASPAR database. ***C***: Schematic illustration of the NFS1 promoter containing TEAD1-binding sites and YY1-binding sites. ***D***: H9C2 cells were treated without or with VP for 48 h. Enrichment for TEAD1 and YY1 at the NFS1 promoter was assessed by RT-qPCR after CUT&RUN assay (n = 6, $^{**}P < 0.01$, $^{***}P < 0.001$ *vs.* CTL). ***E***: H9C2 cells were transfected with CTL-siRNA or YY1-siRNA, and luciferase reporter NFS1 promoter plasmid or control plasmid. ***F***: Western blotting images and quantitative analysis of YY1 and NFS1 in H9C2 cells (n = 6, $^{**}P < 0.01$, $^{***}P < 0.001$ *vs.* CTL-siRNA; $^{\#}P < 0.05$ *vs.* VP + CTL-siRNA). ***G***: Enrichment for TEAD1, YY1 and H3K27me3 at the NFS1 promoter in nTG and Mst1-TG LV tissues was assessed by RT-qPCR after CUT&RUN assay (n = 6 each). $^{***}P < 0.001$ *vs.* respective nTG). ***H***: Western blotting images and quantitative analysis of Src, total YAP (tYAP), nuclear YAP (nYAP), nuclear S127-pYAP, and Y357-pYAP, YY1 and TEAD1 as well as cytoplasmic YAP (cYAP), S127-pYAP and Y357-pYAP in LV tissues (n = 6/group, $^{***}P < 0.001$ *vs.* nTG). ***I***: Representative immunoblots of nuclear protein co-immunoprecipitation for interactions of YAP-TEAD1 and YAP-YY1 in mouse LV tissues. ***J***: Immunofluorescent stain of myocardial sections of LVs from mouse or DCM patients showing the location of YAP (green) and YY1 (red) in cardiomyocyte nuclei, cell nucleus was stained with DAPI. Data are Mean ± SEM.

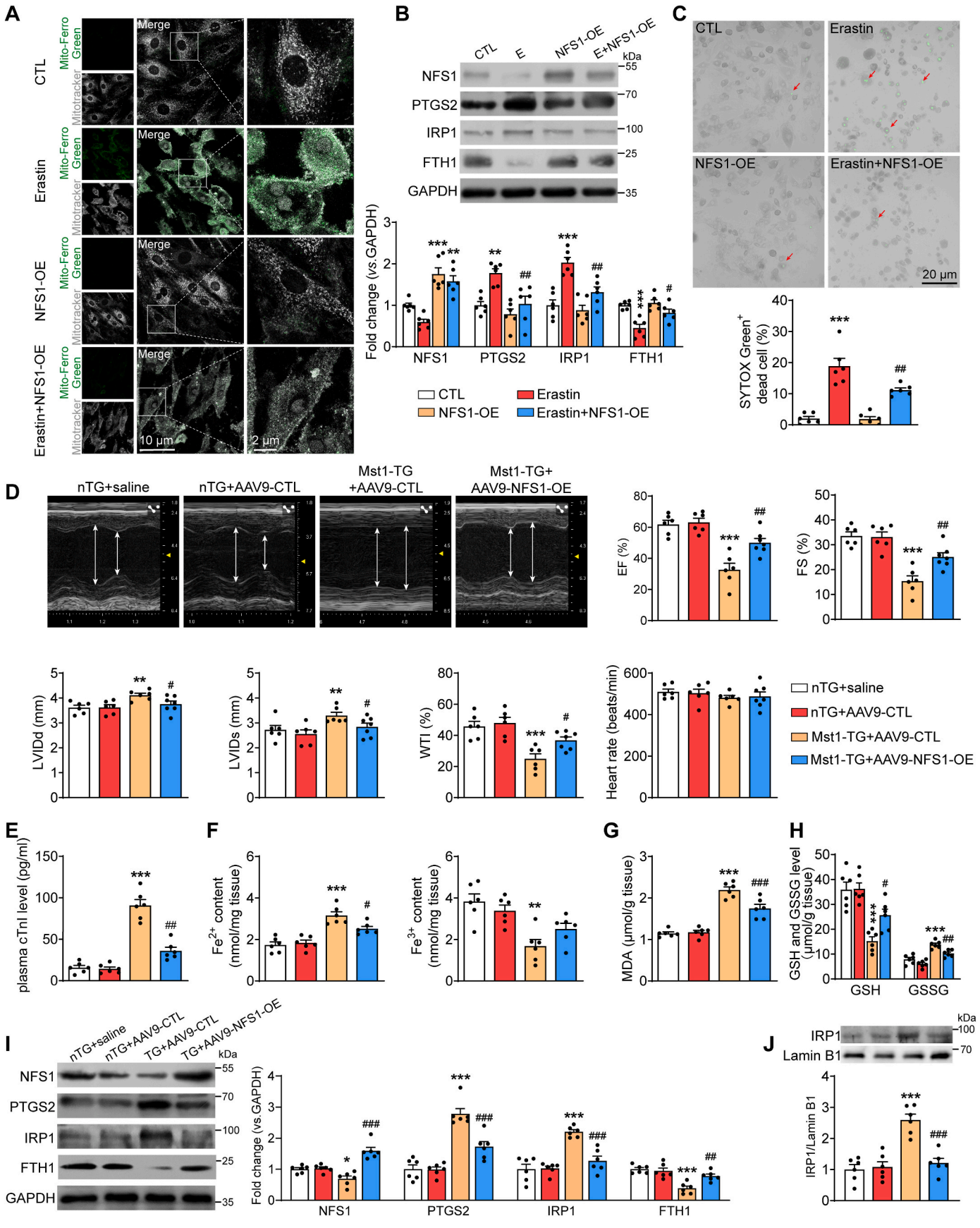

(caption on next page)

Fig. 7. Effect of virally mediated expression of NFS1 on cardiomyocyte ferroptosis in NRVMs treated with erastin or in Mst1-TG mice. In panel A–C: NRVMs were infected with control or NFS1 overexpression adenovirus vector for 24 h, and then treated with or without erastin (0.1 μM) for 24 h. ***A***: Representative Mito-FerroGreen and Mitotracker fluorescence imaging for mitochondrial Fe^{2+}. ***B***: Western blotting images and mean values for marker proteins of ferroptosis and ISC biosynthesis in NRVMs. ***C***: Images and quantitative analysis of SYTOX Green dead cell staining in NRVMs (red arrow). n = 6 dishes/group, $^{**}P < 0.01$, $^{***}P < 0.001$ *vs.* CTL; $^{\#}P < 0.05$, $^{\#\#}P < 0.01$ *vs.* erastin. Panels D–J contain data from 10-week-old nTG and Mst1-TG mice received i.v. injection of saline or 5×10^{11} v.g. AAV9-cTnT-GdGreen or AAV9-cTnT-NFS1-GdGreen for 6 weeks. ***D***: Representative M-mode tracings from short-axis LV 2-D echocardiographic images of mice 6 weeks after the injection. EF, FS, LVIDd, LVIDs, WTI and heart rate were derived from M-mode images. ***E***: Plasma levels of cTnT. ***F***: Labile Fe^{2+} and Fe^{3+} level in LV tissues. ***G***: MDA level in LV tissues. ***H***: GSH and GSSG level in LV tissues. ***I*** and ***J***: Western blotting images and mean values for marker proteins of ferroptosis and ISC biosynthesis and nuclear IRP1 in the mouse LVs. n = 6 each, $^{*}P < 0.05$, $^{**}P < 0.01$, $^{***}P < 0.001$ *vs.* nTG + AAV9-CTL; $^{\#}P < 0.05$, $^{\#\#}P < 0.01$, $^{\#\#\#}P < 0.001$ *vs.* TG + AAV9-CTL. Data are Mean ± SEM.

apoptosis phenotype [25]. Here we observed elevated plasma levels of cTnI or cell death by the SYTOX Green probe, changes that question the apoptosis as a key cell death mode responsible for the progressive cardiomyocyte dropout in this model. Our findings from both Mst1-TG mice and human DCM myocardium suggest that cardiomyocyte ferroptosis plays a key role in the development of DCM. Sustained cardiomyocyte loss induced cardiac remodeling, dysfunction and fibrosis contributing significantly to the initiation and development of cardiomyopathy [33,34]. Closely related to cardiomyocyte ferroptosis is mitochondrial dysfunction and metabolic remodeling that drive the progression of DCM [10]. In the Mst1-TG model, cardiomyopathy phenotype and mitochondrial dysfunction are aligned with clinical characteristics of DCM patients [10,35]. In addition to multiple measurements for ferroptosis, our transcriptome revealed gene profiles suggesting ferroptosis and abnormal iron metabolism in Mst1-TG mouse heart, notably, upregulation of ferroptosis marker genes (*Ptgs2* and *p53*) and iron import genes (*Tfrc* and *Dmt1*), downregulation of genes for iron storage and export, as well as upregulation of *Acsl4* and *Nox4* that are related to lipid peroxidation. These changes at the transcription level were evident in Mst1-TG mouse heart as early as three weeks of age, indicating a causal role of cardiomyocyte ferroptosis in the initiation of cardiomyopathy. By Western blotting, we confirmed similar changes at the protein level for a number of selected genes in the Mst1-TG hearts.

Previous studies have reported the effectiveness in halting ferroptosis by directly targeting Fe^{2+} overload with iron chelators like DFO and dexrazoxane, or lipid peroxidation using antioxidants [36]. In heart disease like doxorubicin-induced cardiomyopathy, DFO was able to reduce cell iron level, thereby alleviating cardiomyocyte ferroptosis [7,37]. Our study demonstrated a pivotal role of Hippo pathway activation in mediating cardiomyocyte ferroptosis and hence becoming a potential target for therapeutic intervention. We found in cultured NRVMs that VP-induced mitochondrial Fe^{2+} overload and ferroptosis was mitigated by treatment with DFO. This finding implied that Hippo pathway activation or YAP-TEAD1 inhibition in cardiomyocytes mediates Fe^{2+} overload. Furthermore, cardiomyocyte ferroptosis and LV dysfunction in Mst1-TG mice were improved by treatment with Fer-1, which is a synthetic antioxidant and a potent inhibitor of ferroptosis through targeting lipid peroxidation [38]. Thus, our findings from the therapeutic interventions using DFO and Fer-1 reinforce a causal role of Hippo pathway activation in inducing cardiomyocyte ferroptosis and its contribution to cardiomyopathy phenotype.

Using an RNA-seq database of human cardiac samples that was published online [32], we obtained evidence indicating activated Hippo pathway in the myocardium of DCM patients. We also found markedly increased ferroptosis indices, such as lipid peroxidation product 4-HNE in LVs of DCM patients. Erastin is a well validated ferroptosis inducer [2]. Interestingly, we found that inactivation of endogenous Mst1 activity using dnMst1-TG model is protective against erastin-induced ferroptosis and LV dysfunction. Similarly, Mst1 knockdown in cultured cardiomyocytes effectively mitigated the adverse effects of erastin like markedly elevated mitochondrial Fe^{2+} levels, lipid peroxidation and cell death. Conversely, treatment with erastin *in vitro* and *in vivo* activated myocardial Hippo pathway evidenced by elevated protein expression and phosphorylation of Mst1. Taking together, our findings unraveled a potential vicious cycle between Hippo pathway activation and ferroptosis that drive the progression of DCM.

Mitochondrion is the important organelle where iron is metabolized primarily for the synthesis of ISCs and heme [1]. We previously reported in the Mst1-TG model significant mitochondrial damage and metabolic reprograming, changes that contribute importantly to cardiomyopathy phenotype [10,24]. Here we further discovered elevation of mitochondrial Fe^{2+} content in cardiomyocytes of Mst1-TG hearts. To define key molecules mediating aberrant metabolism of mitochondrial iron, we analyzed RNA-seq data from Mst1-TG mouse heart as well as published RNA-seq data from human DCM myocardium. In these transcriptomic databases, we identified downregulated genes of ISC biosynthesis in Mst1-TG myocardium, especially ISC assembling genes including *Nfs1*, *Fxn* and *Iscu*. Of note, *Nfs1* was found to be downregulated in mouse cardiomyopathy as well as in myocardial biopsies of human DCM patients. This finding was further validated by protein assay or immunohistochemical staining. ISC is essential cofactor of Fe–S binding proteins involved in multiple cellular processes, including iron homeostasis, energy metabolism and DNA biosynthesis [20,22]. ISC deficiency not only results in metabolic disturbance [39,40], but also evokes the iron-starvation-response with resultant mitochondrial iron accumulation, which is due to nuclear translocation of ISC-unbound aconitase that stabilizes TFRC mRNA but represses translation of FTH1 [41,42]. Indeed, the Mst1-TG myocardium exhibited reduction in the activity of the ISC binding enzyme aconitase and FTH1 protein expression, together with elevated protein abundance of TFRC and nuclear IRP1 protein heart. These findings support the notion that the insufficient ISC biogenesis augments the iron-starvation-response with resultant mitochondrial iron overload.

Being the rate-limiting enzyme in ISC biogenesis, NFS1 harvests sulfur from cysteine and then binds with FXN-carried Fe^{2+} to assemble ISCs on a protein scaffold formed by ISC assembly enzyme (ISCU) [43,44]. In the present study, while downregulation of NFS1 was consistent in the myocardium of both Mst1-TG mice and DCM patients, *FXN* and *ISCU* mRNA levels were moderately upregulated in RNA-seq data of DCM patients but unchanged in Mst1-TG hearts. Such diversities are likely due to differences in species or etiologies. Given that NFS1 knockdown in cardiomyocytes by using NFS1-shRNA induced mitochondrial Fe^{2+} overload and cell death, NFS1 downregulation, in the setting of Hippo pathway activation, would play a central role in cardiomyocyte ferroptosis. In keeping with our finding from the myocardium that suppression of NFS1 induces iron overload and ferroptosis, supportive pieces of evidence are also available from studies in cancer cells showing that suppression of NFS1 sensitizes cancer cells to ferroptosis [22,45], and that patients carrying cancers with high expression of NFS1 were resistant to chemotherapy and had poor survival [23,46].

We provided evidence that NFS1 downregulation is mediated by activation of the Hippo signaling pathway. In NRVMs or the myocardium of nTG mice, treatment with erastin induced ferroptosis, together with NFS1 downregulation and enhanced iron-starvation-response. These effects of erastin were effectively mitigated by Mst1 knockdown in NRVMs, or by transgenic inactivation of Mst1 *in vivo* (dnMst1-TG mice). The downstream signaling was further explored focusing on YAP as the main signal molecule of Hippo pathway via its transcriptional regulation of numerous target genes [14,47], in particular, the involvement of YAP in regulating NFS1 expression. Using the JARSPAR

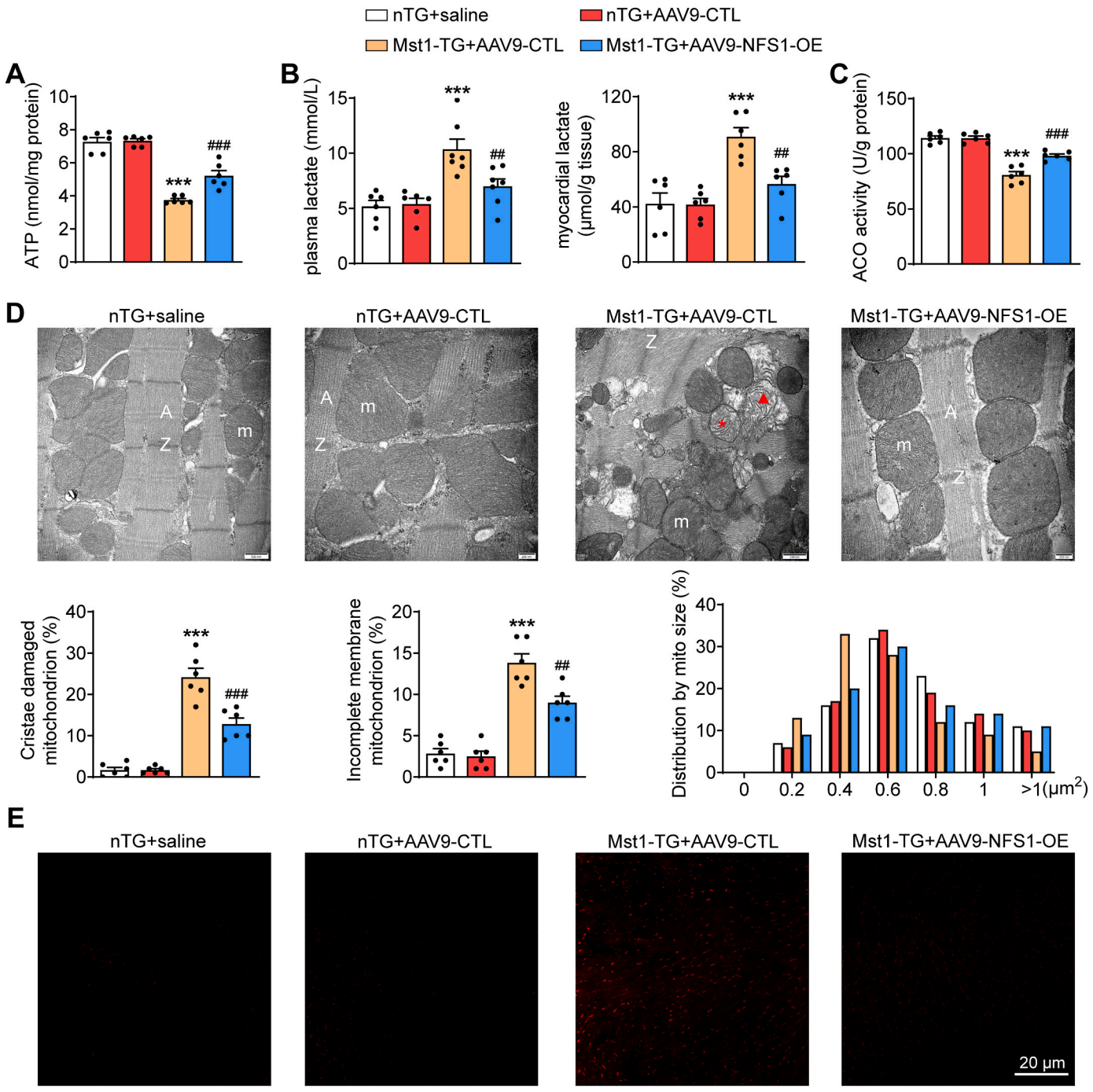

Fig. 8. Effect of myocardial NFS1 restoration on cardiomyocyte mitochondrial function in Mst1-TG mice. ***A***: ATP level in LV tissues. ***B***: Lactate level in plasma and LV tissues. ***C***: Cytoplasmic aconitase activity in LV tissues. ***D***: Electron micrographs showing mitochondria in mouse LV tissues and quantitative analysis of damaged mitochondrion count and distribution of mitochondrial size (n = 3 hearts per group), magnification at 30,000. m: mitochondria; A: A-band; Z: Z-line; *: mitochondria with disrupted cristae; ▲: mitochondria with incomplete outer-membrane. ***E***: Images of DHE staining in LV sections. Data are presented as Mean ± SEM, $^{***}P < 0.001$ *vs.* nTG + AAV9-CTL; $^{\#\#}P < 0.01$, $^{\#\#\#}P < 0.001$ *vs.* TG + AAV9-CTL.

and UCSC database, we predicted and identified both TEAD1 and YY1 as the potential transcriptional factors that interact with YAP and bind to the *Nfs1* promoter. Importantly, the nuclear YAP-TEAD1 interaction was suppressed and the TEAD1 expression was lower in Mst1-TG versus nTG mouse hearts. YY1 is a ubiquitous zinc finger transcription factor and acts as either inducer or repressor for numerous genes by interacting with epigenetic factors to alter DNA methylation or acetylation [48–50]. Our CUT&RUN assay showed that Hippo pathway activation or YAP inactivation was associated with enrichment of both YY1 and H3K27me3 on the *Nfs1* promoter, which was accompanied with dissociation of TEAD1 from the *Nfs1* promoter. H3K27me3-rich genomic regions often represent transcriptional repression [51], and this was confirmed by our luciferase reporter assay or Western blotting showing transcriptional suppression of *Nfs1*. Furthermore, YAP-TEAD1 inhibition using VP similarly repressed NFS1 expression, and this effect of VP was partially restored by YY1 gene silencing. Thus, YAP-YY1 interaction represses *Nfs1* expression. Although Mst1 overexpression induced canonical Hippo pathway activation with an elevated Ser127-pYAP level, we found that nuclear YAP level was increased in the Mst1-TG myocardium. This implies that factor(s) other than

Ser127-phosphoryltion also regulates YAP nuclear entry and its transcriptional activity. Indeed, we found in Mst1-TG hearts increased expression of Src, a kinase known to phosphorylate YAP at Tyr357, leading to enhanced YAP nuclear translocation [12,13]. Using nuclear protein fraction from Mst1-TG hearts, we found that protein abundance of both YY1 and YAP-YY1 interaction increased, but that of TEAD1 and YAP-TEAD1 interaction decreased. Importantly, enhanced YAP-YY1 interaction was similarly observed in the nuclei of LV tissues from DCM patients. These findings support a working model by which activity of the *Nfs1* promoter is counter-regulated by binding to YAP-TEAD1 (activator) or YAP-YY1 (repressor), resulting in the reciprocal changes in the abundance of promoter DNA methylation (graphical abstract and Fig. 6G). As far as we are aware, this is the first report on the transcriptional suppression by Hippo pathway of NFS1 expression that involves YAP-YY1, and ISC biosynthesis, ultimately facilitating cardiomyocyte ferroptosis.

Finally, in cultured NRVMs or in Mst1-TG mice, we examined the effects of virally-mediated expression of NFS1 on ferroptotic markers, cardiomyopathy phenotype and mitochondrial function. Viral infection restored NFS1 expression (by 75 % vs. control NRVMs, or by 1.29-fold vs. Mst1-TG+AAV-controls), and significantly mitigated ferroptosis markers in both erastin-treated NRVMs or in Mst1-TG mice. Furthermore, restoration of NFS1 expression in Mst1-TG mice improved LV function together with partial amelioration in ultrastructure and function of mitochondria estimated by EM imaging, or by a range of assays for ATP, lactate, ROS production and aconitase activity. Thus, in our DCM model with Hippo pathway activation, maintenance of cardiomyocyte NFS1 expression holds the promise to be developed into a therapeutic strategy to ameliorate myocardial ferroptosis and cardiomyopathy. This finding might bear clinical implication given that cardiac Hippo pathway activation is evident in patients with different types of cardiomyopathy and heart failure [16,17].

In conclusion, the present study demonstrated that myocardial Hippo pathway activation promotes development of DCM at least in a large part by inducing cardiomyocyte ferroptosis. The mechanism of ferroptosis involves transcriptional repression of NFS1 due to the imbalanced binding to the *Nfs1* promoter by TEAD1 and YY1, a process regulated by nuclear YAP. Downregulation of NFS1 diminishes ISC biosynthesis and evokes the iron-starvation-response, leading to iron overload and ferroptosis. We provided experimental evidence for maintenance of cardiomyocyte NFS1 level as a novel therapeutic approach to protect against cardiomyocyte ferroptosis and DCM in the setting of Hippo pathway activation.

CRediT authorship contribution statement

Gang She: Writing – review & editing, Writing – original draft, Visualization, Validation, Project administration, Methodology, Investigation, Funding acquisition, Formal analysis, Data curation, Conceptualization. **Xia-Xia Hai:** Methodology, Investigation, Formal analysis. **Li-Ye Jia:** Methodology, Investigation, Formal analysis, Data curation. **Yong-Jian Zhang:** Resources. **Yu-Jie Ren:** Resources. **Zheng-Da Pang:** Methodology. **Lin-Hong Wu:** Investigation. **Meng-Zhuan Han:** Methodology. **Yu Zhang:** Investigation. **Jing-Jing Li:** Methodology. **Ru-Yue Bai:** Investigation. **Bao-Chang Lai:** Methodology. **Yi-Yi Yang:** Validation. **Junichi Sadoshima:** Resources. **Xiao-Jun Du:** Writing – review & editing, Writing – original draft, Supervision, Resources, Project administration, Conceptualization. **Xiu-Ling Deng:** Writing – review & editing, Supervision. **Yi Zhang:** Writing – review & editing, Supervision.

Ethics approval statement and consent to participate

All animal experimental procedures were approved by the Biomedical Animal Ethics Committee of Health Science Center, Xi'an Jiaotong University carried out following their legal requirements (No. 2022-624). LV tissues of human DCM patients were used with written informed consent from patients prior to participation in the study. This study was approved by the Ethics Committee of the first affiliated Hospital of Xi'an Jiaotong University (No. LLSBPJ-2024-003).

Sources of funding

This work was supported by the National Natural Science Foundation of China (82200332), the China Postdoctoral Science Foundation (2023T160518) and the Fundamental Research Funds for the Central Universities of Xi'an Jiaotong University (xzy012024095).

Declaration of competing interest

The authors declare that they have no known competing financial interests or personal relationships that could have appeared to influence the work reported in this paper.

Acknowledgments

None.

Appendix A. Supplementary data

Supplementary data to this article can be found online at https://doi.org/10.1016/j.redox.2025.103597.

Data availability

Data will be made available on request.

References

[1] X. Fang, H. Ardehali, J. Min, F. Wang, The molecular and metabolic landscape of iron and ferroptosis in cardiovascular disease, Nat. Rev. Cardiol. 20 (2023) 7–23, https://doi.org/10.1038/s41569-022-00735-4.
[2] X. Jiang, B.R. Stockwell, M. Conrad, Ferroptosis: mechanisms, biology and role in disease, Nat. Rev. Mol. Cell Biol. 22 (2021) 266–282, https://doi.org/10.1038/s41580-020-00324-8.
[3] M. Gao, J. Yi, J. Zhu, A.M. Minikes, P. Monian, C.B. Thompson, X. Jiang, Role of mitochondria in ferroptosis, Mol. Cell 73 (2019) 354–363, https://doi.org/10.1016/j.molcel.2018.10.042, e353.
[4] S.Y. Sheng, J.M. Li, X.Y. Hu, Y. Wang, Regulated cell death pathways in cardiomyopathy, Acta Pharmacol. Sin. 44 (2023) 1521–1535, https://doi.org/10.1038/s41401-023-01068-9.
[5] X. Wu, Y. Li, S. Zhang, X. Zhou, Ferroptosis as a novel therapeutic target for cardiovascular disease, Theranostics 11 (2021) 3052–3059, https://doi.org/10.7150/thno.54113.
[6] L. Wu, Y. Zhang, G. Wang, J. Ren, Molecular mechanisms and therapeutic targeting of ferroptosis in doxorubicin-induced cardiotoxicity, JACC Basic Transl Sci 9 (2024) 811–826, https://doi.org/10.1016/j.jacbts.2023.10.009.
[7] T. Tadokoro, M. Ikeda, T. Ide, H. Deguchi, S. Ikeda, K. Okabe, A. Ishikita, S. Matsushima, T. Koumura, K.I. Yamada, et al., Mitochondria-dependent ferroptosis plays a pivotal role in doxorubicin cardiotoxicity, JCI Insight 5 (2020) e132747, https://doi.org/10.1172/jci.insight.132747.
[8] J. Wang, S. Liu, T. Heallen, J.F. Martin, The Hippo pathway in the heart: pivotal roles in development, disease, and regeneration, Nat. Rev. Cardiol. 15 (2018) 672–684, https://doi.org/10.1038/s41569-018-0063-3.
[9] F.X. Yu, B. Zhao, K.L. Guan, Hippo pathway in organ size control, tissue homeostasis, and cancer, Cell 163 (2015) 811–828, https://doi.org/10.1016/j.cell.2015.10.044.
[10] W. Wu, M. Ziemann, K. Huynh, G. She, Z.D. Pang, Y. Zhang, T. Duong, H. Kiriazis, T.T. Pu, R.Y. Bai, et al., Activation of Hippo signaling pathway mediates mitochondria dysfunction and dilated cardiomyopathy in mice, Theranostics 11 (2021) 8993–9008, https://doi.org/10.7150/thno.62302.
[11] F. Zanconato, M. Cordenonsi, S. Piccolo, YAP and TAZ: a signalling hub of the tumour microenvironment, Nat. Rev. Cancer 19 (2019) 454–464, https://doi.org/10.1038/s41568-019-0168-y.
[12] B. Li, J. He, H. Lv, Y. Liu, X. Lv, C. Zhang, Y. Zhu, D. Ai, c-Abl regulates YAPY357 phosphorylation to activate endothelial atherogenic responses to disturbed flow, J. Clin. Investig. 129 (2019) 1167–1179, https://doi.org/10.1172/JCI122440.
[13] F. Haderk, Y.T. Chou, L. Cech, C. Fernandez-Mendez, J. Yu, V. Olivas, I.M. Meraz, D. Barbosa Rabago, D.L. Kerr, C. Gomez, et al., Focal adhesion kinase-YAP signaling axis drives drug-tolerant persister cells and residual disease in lung cancer, Nat. Commun. 15 (2024) 3741, https://doi.org/10.1038/s41467-024-47423-0.

[14] G. She, J.C. Du, W. Wu, T.T. Pu, Y. Zhang, R.Y. Bai, Y. Zhang, Z.D. Pang, H. F. Wang, Y.J. Ren, et al., Hippo pathway activation mediates chemotherapy-induced anti-cancer effect and cardiomyopathy through causing mitochondrial damage and dysfunction, Theranostics 13 (2023) 560–577, https://doi.org/10.7150/thno.79227.
[15] R. Liu, R. Jagannathan, L. Sun, F. Li, P. Yang, J. Lee, V. Negi, E.M. Perez-Garcia, S. Shiva, V.K. Yechoor, et al., Tead1 is essential for mitochondrial function in cardiomyocytes, Am. J. Physiol. Heart Circ. Physiol. 319 (2020) H89–H99, https://doi.org/10.1152/ajpheart.00732.2019.
[16] J.P. Leach, T. Heallen, M. Zhang, M. Rahmani, Y. Morikawa, M.C. Hill, A. Segura, J.T. Willerson, J.F. Martin, Hippo pathway deficiency reverses systolic heart failure after infarction, Nature 550 (2017) 260–264, https://doi.org/10.1038/nature24045.
[17] N. Hou, Y. Wen, X. Yuan, H. Xu, X. Wang, F. Li, B. Ye, Activation of Yap1/Taz signaling in ischemic heart disease and dilated cardiomyopathy, Exp. Mol. Pathol. 103 (2017) 267–275, https://doi.org/10.1016/j.yexmp.2017.11.006.
[18] M.M. Mia, M.K. Singh, The hippo signaling pathway in cardiac development and diseases, Front. Cell Dev. Biol. 7 (2019) 211, https://doi.org/10.3389/fcell.2019.00211.
[19] S. Ahola, T. Langer, Ferroptosis in mitochondrial cardiomyopathy, Trends Cell Biol. 34 (2024) 150–160, https://doi.org/10.1016/j.tcb.2023.06.002.
[20] O. Stehling, C. Wilbrecht, R. Lill, Mitochondrial iron-sulfur protein biogenesis and human disease, Biochimie 100 (2014) 61–77, https://doi.org/10.1016/j.biochi.2014.01.010.
[21] A.D. Read, R.E. Bentley, S.L. Archer, K.J. Dunham-Snary, Mitochondrial iron-sulfur clusters: structure, function, and an emerging role in vascular biology, Redox Biol. 47 (2021) 102164, https://doi.org/10.1016/j.redox.2021.102164.
[22] S.W. Alvarez, V.O. Sviderskiy, E.M. Terzi, T. Papagiannakopoulos, A.L. Moreira, S. Adams, D.M. Sabatini, K. Birsoy, R. Possemato, NFS1 undergoes positive selection in lung tumours and protects cells from ferroptosis, Nature 551 (2017) 639–643, https://doi.org/10.1038/nature24637.
[23] J.F. Lin, P.S. Hu, Y.Y. Wang, Y.T. Tan, K. Yu, K. Liao, Q.N. Wu, T. Li, Q. Meng, J. Z. Lin, et al., Phosphorylated NFS1 weakens oxaliplatin-based chemosensitivity of colorectal cancer by preventing PANoptosis, Signal Transduct. Targeted Ther. 7 (2022) 54, https://doi.org/10.1038/s41392-022-00889-0.
[24] M.N. Nguyen, M. Ziemann, H. Kiriazis, Y. Su, Z. Thomas, Q. Lu, D.G. Donner, W. B. Zhao, H. Rafehi, J. Sadoshima, et al., Galectin-3 deficiency ameliorates fibrosis and remodeling in dilated cardiomyopathy mice with enhanced Mst1 signaling, Am. J. Physiol. Heart Circ. Physiol. 316 (2019) H45–H60, https://doi.org/10.1152/ajpheart.00609.2018.
[25] S. Yamamoto, G. Yang, D. Zablocki, J. Liu, C. Hong, S.J. Kim, S. Soler, M. Odashima, J. Thaisz, G. Yehia, et al., Activation of Mst1 causes dilated cardiomyopathy by stimulating apoptosis without compensatory ventricular myocyte hypertrophy, J. Clin. Investig. 111 (2003) 1463–1474, https://doi.org/10.1172/JCI17459.
[26] X. Fang, Z. Cai, H. Wang, D. Han, Q. Cheng, P. Zhang, F. Gao, Y. Yu, Z. Song, Q. Wu, et al., Loss of cardiac ferritin H facilitates cardiomyopathy via slc7a11-mediated ferroptosis, Circ. Res. 127 (2020) 486–501, https://doi.org/10.1161/CIRCRESAHA.120.316509.
[27] A.V. Menon, J. Liu, H.P. Tsai, L. Zeng, S. Yang, A. Asnani, J. Kim, Excess heme upregulates heme oxygenase 1 and promotes cardiac ferroptosis in mice with sickle cell disease, Blood 139 (2022) 936–941, https://doi.org/10.1182/blood.2020008455.
[28] G. She, M.C. Hou, Y. Zhang, Y. Zhang, Y. Wang, H.F. Wang, B.C. Lai, W.B. Zhao, X. J. Du, X.L. Deng, Gal-3 (Galectin-3) and KCa3.1 mediate heterogeneous cell coupling and myocardial fibrogenesis driven by betaAR (beta-Adrenoceptor) activation, Hypertension 75 (2020) 393–404, https://doi.org/10.1161/HYPERTENSIONAHA.119.13696.
[29] X.J. Du, L. Fang, X.M. Gao, H. Kiriazis, X. Feng, E. Hotchkin, A.M. Finch, H. Chaulet, R.M. Graham, Genetic enhancement of ventricular contractility protects against pressure-overload-induced cardiac dysfunction, J. Mol. Cell. Cardiol. 37 (2004) 979–987, https://doi.org/10.1016/j.yjmcc.2004.07.010.
[30] M. Chaffin, I. Papangeli, B. Simonson, A.D. Akkad, M.C. Hill, A. Arduini, S. J. Fleming, M. Melanson, S. Hayat, M. Kost-Alimova, et al., Single-nucleus profiling of human dilated and hypertrophic cardiomyopathy, Nature 608 (2022) 174–180, https://doi.org/10.1038/s41586-022-04817-8.
[31] G. She, Y.J. Ren, Y. Wang, M.C. Hou, H.F. Wang, W. Gou, B.C. Lai, T. Lei, X.J. Du, X.L. Deng, KCa3.1 channels promote cardiac fibrosis through mediating inflammation and differentiation of monocytes into myofibroblasts in angiotensin II -treated rats, J. Am. Heart Assoc. 8 (2019) e010418, https://doi.org/10.1161/JAHA.118.010418.
[32] M.E. Sweet, A. Cocciolo, D. Slavov, K.L. Jones, J.R. Sweet, S.L. Graw, T.B. Reece, A. V. Ambardekar, M.R. Bristow, L. Mestroni, et al., Transcriptome analysis of human heart failure reveals dysregulated cell adhesion in dilated cardiomyopathy and activated immune pathways in ischemic heart failure, BMC Genom. 19 (2018) 812, https://doi.org/10.1186/s12864-018-5213-9.
[33] E.M. McNally, L. Mestroni, Dilated cardiomyopathy: genetic determinants and mechanisms, Circ. Res. 121 (2017) 731–748, https://doi.org/10.1161/CIRCRESAHA.116.309396.
[34] H.P. Schultheiss, D. Fairweather, A.L.P. Caforio, F. Escher, R.E. Hershberger, S. E. Lipshultz, P.P. Liu, A. Matsumori, A. Mazzanti, J. McMurray, et al., Dilated cardiomyopathy, Nat. Rev. Dis. Primers 5 (2019) 32, https://doi.org/10.1038/s41572-019-0084-1.
[35] S. Heymans, N.K. Lakdawala, C. Tschope, K. Klingel, Dilated cardiomyopathy: causes, mechanisms, and current and future treatment approaches, Lancet 402 (2023) 998–1011, https://doi.org/10.1016/S0140-6736(23)01241-2.
[36] D. Tang, X. Chen, R. Kang, G. Kroemer, Ferroptosis: molecular mechanisms and health implications, Cell Res. 31 (2021) 107–125, https://doi.org/10.1038/s41422-020-00441-1.
[37] Y. Ichikawa, M. Ghanefar, M. Bayeva, R. Wu, A. Khechaduri, S.V. Naga Prasad, R. K. Mutharasan, T.J. Naik, H. Ardehali, Cardiotoxicity of doxorubicin is mediated through mitochondrial iron accumulation, J. Clin. Investig. 124 (2014) 617–630, https://doi.org/10.1172/JCI72931.
[38] G. Miotto, M. Rossetto, M.L. Di Paolo, L. Orian, R. Venerando, A. Roveri, A. M. Vuckovic, V. Bosello Travain, M. Zaccarin, L. Zennaro, et al., Insight into the mechanism of ferroptosis inhibition by ferrostatin-1, Redox Biol. 28 (2020) 101328, https://doi.org/10.1016/j.redox.2019.101328.
[39] T.A. Rouault, Biogenesis of iron-sulfur clusters in mammalian cells: new insights and relevance to human disease, Dis Model Mech 5 (2012) 155–164, https://doi.org/10.1242/dmm.009019.
[40] N.P. Ward, Y.P. Kang, A. Falzone, T.A. Boyle, G.M. DeNicola, Nicotinamide nucleotide transhydrogenase regulates mitochondrial metabolism in NSCLC through maintenance of Fe-S protein function, J. Exp. Med. 217 (2020) e20191689, https://doi.org/10.1084/jem.20191689.
[41] E.M. Terzi, V.O. Sviderskiy, S.W. Alvarez, G.C. Whiten, R. Possemato, Iron-sulfur cluster deficiency can be sensed by IRP2 and regulates iron homeostasis and sensitivity to ferroptosis independent of IRP1 and FBXL5, Sci. Adv. 7 (2021) eabg4302, https://doi.org/10.1126/sciadv.abg4302.
[42] T.A. Rouault, The role of iron regulatory proteins in mammalian iron homeostasis and disease, Nat. Chem. Biol. 2 (2006) 406–414, https://doi.org/10.1038/nchembio807.
[43] R. Lill, S.A. Freibert, Mechanisms of mitochondrial iron-sulfur protein biogenesis, Annu. Rev. Biochem. 89 (2020) 471–499, https://doi.org/10.1146/annurev-biochem-013118-111540.
[44] M. Zhang, Z. Liu, Y. Le, Z. Gu, H. Zhao, Iron-sulfur clusters: a key factor of regulated cell death in cancer, Oxid. Med. Cell. Longev. 2022 (2022) 7449941, https://doi.org/10.1155/2022/7449941.
[45] Q. Zhou, Y. Meng, D. Li, L. Yao, J. Le, Y. Liu, Y. Sun, F. Zeng, X. Chen, G. Deng, Ferroptosis in cancer: from molecular mechanisms to therapeutic strategies, Signal Transduct. Targeted Ther. 9 (2024) 55, https://doi.org/10.1038/s41392-024-01769-5.
[46] K.M. Fujihara, B.Z. Zhang, T.D. Jackson, M.O. Ogunkola, B. Nijagal, J.V. Milne, D. A. Sallman, C.S. Ang, I. Nikolic, C.J. Kearney, et al., Eprenetapopt triggers ferroptosis, inhibits NFS1 cysteine desulfurase, and synergizes with serine and glycine dietary restriction, Sci. Adv. 8 (2022) eabm9427, https://doi.org/10.1126/sciadv.abm9427.
[47] Q. Zhou, L. Li, B. Zhao, K.L. Guan, The hippo pathway in heart development, regeneration, and diseases, Circ. Res. 116 (2015) 1431–1447, https://doi.org/10.1161/CIRCRESAHA.116.303311.
[48] I.T.S. Meliala, R. Hosea, V. Kasim, S. Wu, The biological implications of Yin Yang 1 in the hallmarks of cancer, Theranostics 10 (2020) 4183–4200, https://doi.org/10.7150/thno.43481.
[49] S. Hoxha, A. Shepard, S. Troutman, H. Diao, J.R. Doherty, M. Janiszewska, R. M. Witwicki, M.E. Pipkin, W.W. Ja, M.S. Kareta, et al., YAP-mediated recruitment of YY1 and EZH2 represses transcription of key cell-cycle regulators, Cancer Res. 80 (2020) 2512–2522, https://doi.org/10.1158/0008-5472.CAN-19-2415.
[50] Y. Ning, H.M. Zheng, Y. Yang, H.J. Zang, W.Y. Wang, Y.T. Zhan, H.H. Wang, J. D. Luo, Q.Y. Wen, J.W. Peng, et al., YAP1 synergize with YY1 transcriptional co-repress DUSP1 to induce osimertinib resistant by activating the EGFR/MAPK pathway and abrogating autophagy in non-small cell lung cancer, Int. J. Biol. Sci. 19 (2023) 2458–2474, https://doi.org/10.7150/ijbs.79965.
[51] Y. Cai, Y. Zhang, Y.P. Loh, J.Q. Tng, M.C. Lim, Z. Cao, A. Raju, E. Lieberman Aiden, S. Li, L. Manikandan, et al., H3K27me3-rich genomic regions can function as silencers to repress gene expression via chromatin interactions, Nat. Commun. 12 (2021) 719, https://doi.org/10.1038/s41467-021-20940-y.